

Eva Kremshofer, Bsc.

TEM investigation of the structural and chemical order of lead-free piezoelectric alkali bismuth titanates

MASTER THESIS

For obtaining the academic degree
Diplom-Ingenieurin

Master Programme of
Advanced Materials Science



Graz University of Technology

Supervisor:

Ao.Univ.-Prof. Dipl.-Ing. Dr.techn. Werner Grogger
Institute for Electron Microscopy


Graz, December 2010

Deutsche Fassung:
Beschluss der Curricula-Kommission für Bachelor-, Master- und Diplomstudien vom 10.11.2008
Genehmigung des Senates am 1.12.2008

EIDESSTÄTTLICHE ERKLÄRUNG

Ich erkläre an Eides statt, dass ich die vorliegende Arbeit selbstständig verfasst, andere als die angegebenen Quellen/Hilfsmittel nicht benutzt, und die den benutzten Quellen wörtlich und inhaltlich entnommene Stellen als solche kenntlich gemacht habe.

Graz, am 14.12.2010

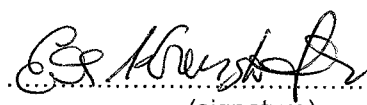

.....
(Unterschrift)

Englische Fassung:

STATUTORY DECLARATION

I declare that I have authored this thesis independently, that I have not used other than the declared sources / resources, and that I have explicitly marked all material which has been quoted either literally or by content from the used sources.

14.12.2010
.....
date


.....
(signature)

Abstract

In 2006, the EU-directive 2002/95/EG for the restriction of hazardous substances (RoHS) in electric and electronic devices was enforced. Among these substances is lead, which is widely used in ferro- and piezoelectric ceramics such as lead zirconate titanate (PZT). PZT is the standard material for piezoelectrics and is used for actuators and sensors, e.g. in automotive applications. Due to the mentioned restrictions, research for lead-free alternatives has been intensified in recent years.

In the present work, two bismuth sodium titanate systems were investigated by means of transmission electron microscopy (TEM). The determination of the crystal structure had been intended before, but a clear correlation to one crystal system was not possible. Therefore, and due to the possibility of investigation of the local homogeneity of the crystal structure, single crystal samples were investigated using TEM. Furthermore, the homogeneity of the chemical elements in the samples was investigated by means of analytical methods in TEM.

On the basis of electron diffraction in TEM, the crystal structure of the samples could be determined, the lattice parameters could be calculated and conclusions concerning the structural homogeneity of the samples could be drawn. In one of the samples, domain-like structures were revealed. These domains were investigated by means of selected area electron diffraction, dark field imaging and high-resolution TEM. Regarding the distribution of the chemical elements, it was shown that the samples were homogeneous to a large extent in the examined areas.

Kurzfassung

2006 trat die EU-Richtlinie 2002/95/EG zur Beschränkung der Verwendung bestimmter gefährlicher Stoffe (RoHS - Restriction of Hazardous Substances) in Kraft, eine Verordnung, die die Verwendung von einigen Substanzen im Bereich Elektro- und Elektronikgeräte beschränkt bzw. verbietet. Darunter ist auch Blei, das in ferro- und piezoelektrischen Keramiken wie Blei-Zirkonat-Titanat (PZT) breite Verwendung als Aktuatoren und Sensoren z.B. im Automobilbereich findet. Aufgrund dieser Beschränkungen wurden die Forschungen an bleifreien Systemen in den letzten Jahren intensiviert.

In der vorliegenden Arbeit wurden zwei auf Bismuth-Natrium-Titanat basierte Systeme im Transmissionselektronenmikroskop (TEM) untersucht. Eine Bestimmung der Kristallstruktur war zuvor mit Röntgendiffraktometrie angestrebt worden, eine eindeutige Zuordnung zu einem Kristallsystem war aber nicht möglich. In dieser Arbeit wurden daher einkristalline Proben im TEM untersucht, auch, weil dadurch die Untersuchung der Homogenität bezüglich der Kristallstruktur möglich ist. Weiters wurde mittels analytischer Verfahren im TEM untersucht, ob die chemischen Elemente homogen in den Proben verteilt sind.

Anhand von Elektronenbeugung im TEM konnten die Kristallstruktur der Proben ermittelt und die Gitterparameter berechnet werden, ebenso konnten Aussagen zur strukturellen Homogenität der Proben gemacht werden. In einer der beiden Proben wurden außerdem interessante, domänenartige Strukturen entdeckt, die mittels Feinbereichselektronenbeugung, Dunkelfeldbildern und Hochauflösungs-TEM näher untersucht wurden. Bezüglich der Verteilung der chemischen Elemente konnte gezeigt werden, dass die Proben in den betrachteten Bereichen weitgehend homogen sind.

Acknowledgment

First of all I would like to express my thanks to my supervisor Werner Grogger for his support and the fruitful discussions throughout this work as well as to Ilse Letofsky-Papst for always being receptive for all my questions and problems.

Furthermore I would like to thank Prof. Ferdinand Hofer for providing the opportunity to carry out my master thesis at the Institute for Electron Microscopy and Prof. Klaus Reichmann from the Institute of Chemical Technology of Materials whose area of expertise the thesis' topic originates from, and Denis Orosel who provided the samples and X-ray measurements.

I would also like to thank Manuel, Daniel and Sebastian for assistance in preparing my specimens.

Special thanks to Christian Gspan for his helping hand concerning the practical work at the electron microscopes and to Mihaela Albu for assistance with the analytical measurements.

Not to forget all the other colleagues of the institute who provided for a pleasant working atmosphere.

Furthermore I would like to express my gratitude to Vicki Keast for proofreading my thesis.

Last but not least my thanks go to my parents who always supported my studies and to Michael for his helping hand whenever I needed advice or encouragement.

Contents

1	Motivation	6
2	Material	8
2.1	The piezoelectric effect	8
2.2	Standard materials for piezoelectric applications	10
2.3	The way to lead-free, piezoelectric materials	13
2.4	Types of lead-free piezoelectric ceramics	14
2.4.1	Classification due to crystal structures	14
2.4.2	Classification due to the chemical composition	17
3	Methods	21
3.1	The Transmission Electron Microscope (TEM)	21
3.2	The assembly of a TEM	22
3.2.1	The electron gun	22
3.2.2	The illumination system	23
3.2.3	The imaging system	24
3.3	Operation modes	26
3.3.1	Electron Diffraction	26
3.3.2	Imaging Mode	27
3.4	Chemical analysis in a TEM	29
3.4.1	The EEL spectrum	29
3.4.2	The EDX spectrum	30
4	Specimen	32
4.1	Specimen preparation using the mixed oxide method	32
4.2	Specimen preparation for investigation in TEM	33
5	Investigation in TEM	35
5.1	Transmission Electron Microscopes	35
5.1.1	FEI Tecnai 12 (T 12)	35
5.1.2	Philips CM 20	35
5.1.3	FEI Tecnai F 20 (TF 20)	36
5.2	Investigation of $(\text{Bi}_{0.5}, \text{Na}_{0.5})\text{TiO}_3\text{-BaTiO}_3$	38

Contents

5.2.1	Powder electron diffraction	39
5.2.2	Single crystal electron diffraction	43
5.2.3	Chemical analysis of BNT-6BT	46
5.3	Investigation of $(\text{Bi}_{0.5}\text{Na}_{0.35}\text{Li}_{0.15})\text{TiO}_3$	52
5.3.1	Powder electron diffraction	52
5.3.2	Single crystal electron diffraction	54
5.3.3	Chemical analysis of BNT-15BLT	62
6	Summary	68

1 Motivation

Today, the standard material for piezoelectric applications is the ceramic material lead zirconate titanate (PZT). In 2003, however, the European Union published the so called *Restriction of Hazardous Substances Directive* (RoHS) which was enforced in 2006 [1]. The directive restricts the use of several hazardous substances, one of which is lead. Though lead-free piezoelectric materials were discovered at approximately the same time as PZT, the effort in research on lead-free piezoelectric materials has been increased in recent years due to the mentioned directive. Bismuth alkali titanates are one group of materials with promising properties. Nevertheless, lead-free materials are not yet ready for use in a wide range of applications.

The present work deals with two groups of bismuth alkali titanates: a binary system of bismuth sodium titanate and barium titanate and a binary system of bismuth sodium titanate and bismuth lithium titanate. In both cases, the system bismuth sodium titanate (BNT) has been altered by adding an element which is supposed to occupy A-sites, but differs in size compared to the other A-site ions of the system, sodium and bismuth. With the addition of barium, a larger ion has been introduced, while lithium is smaller in size. Due to their difference in size, barium and lithium are expected to distort the unit cell to a different extent.

X-ray powder diffraction measurements in earlier works have not provided clear results concerning the crystal structure, because the diffraction patterns allowed interpretation with two different crystal structure models. Therefore, single crystal samples were investigated by means of transmission electron microscopy in this work in order to determine the crystal structure of the materials and the effect of doping with ions of different sizes.

Furthermore, the composition of one of the materials is located at a so called morphotropic phase boundary (MPB), i.e. a certain composition which separates two crystal systems. In most cases, however, the MPB is not characterized by a narrow line, but rather by a compositional range. Hence, another task regards the investigation of homogeneity concerning the crystal structure of the material and the question whether

the sample consists of just one crystal structure or if eventually the coexistence of two phases can be revealed. In addition to the local crystal structure, the examination of the local chemical composition is of interest.

2 Material

2.1 The piezoelectric effect

This chapter is based on references [2] and [3].

When a mechanical force is applied on a piezoelectric material, an electric field is generated by this material as response to the force. This phenomenon is known as the direct piezoelectric effect. On the other hand, the inverse piezoelectric effect describes the behaviour of the material in an electric field where it changes its dimensions. For example, strain or compression applied to a discoid sample with electrodes on both the upper and the lower surface result in a current flow in the case of a closed circuit. The only difference between those two cases is the sign. An electric field applied to the sample will result in a strain or a compression of the sample, depending on the direction of the field. This is depicted in Figure 1.

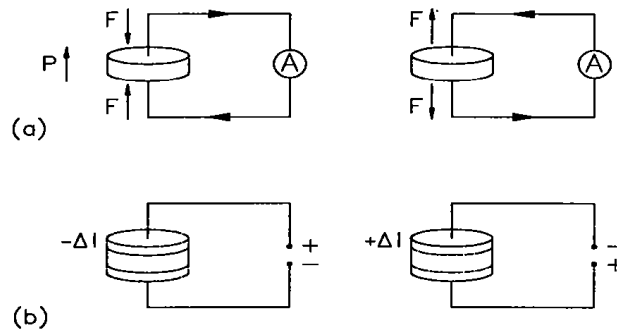


Figure 1: Direct (a) and inverse (b) piezoelectric effect

Both an electric field and a mechanical force introduce polarisation in the sample which means a displacement of the ions against each other. Crystallographic point groups with an inversion center show a symmetrical displacement. Hence, the dipole moments compensate each other and the resulting dipole moment is zero. Therefore, materials with these point groups do not show any piezoelectric effect. However, 21 out of the 32 point groups do not have an inversion center. One of them represents a primitive

unit cell which does not show this effect either. The remaining 20 point groups respond to an applied electric field with a displacement of the ions and therefore a resulting dipole moment other than zero. To sum up, 20 of the existing 32 point groups show the piezoelectric effect.

The following equations of piezoelectricity show that a deformation can be achieved not only in a mechanical way, but also with an electric field (see Equation 2). On the other hand, a dielectric displacement can be achieved via a deformation of the sample in addition to the conventional way, i.e. an electric field (see Equation 1). Equation 1 describes direct piezoelectricity, Equation 2 the inverse case. In the equations, S equates to deformation, D to dielectric displacement, E to the electric field and T to the mechanical stress; s is the elastic compliance, ε the permittivity and d the piezoelectric coefficient.

$$D = d \cdot T + \varepsilon \cdot E \quad (1)$$

$$S = d \cdot E + s \cdot T \quad (2)$$

Another important parameter is the coupling coefficient k . It is a measure of the conversion of electrical to mechanical energy and vice versa which means that k describes the efficiency of the conversion.

The requirements to a piezoelectric ceramic are summarized as follows (though certain parameters are more or less important, depending on the application): ferroelectric behaviour, a high Curie temperature T_C as well as a high depoling temperature T_d are required to allow for applications in a wide temperature range. Temperatures up to 200°C, for example, are reached in applications in the automotive field. For a large piezoelectric effect, a large piezoelectric constant and a high remanent polarisation P_r are desirable. To achieve a high efficiency a high coupling coefficient is required. To minimise energy loss due to hysteresis during poling, the coercive field E_c needs to be small. Some of these parameters are shown in Table 1 for two commercially available examples of a lead zirconate titanate (PZT) ceramic sold by the company *PI Ceramic* [4].

Table 1: Piezoelectric parameters for two examples of a soft piezoelectric PZT material [4]

Type	PIC 151	PIC 155
Curie temperature T_C	250	345
coupling coefficient k_{33}	0.69	0.69
piezoelectric coefficient d_{33}	500	360

An important property of piezoelectric materials is the formation of domains. Due to the transition from a paraelectric to a ferroelectric phase the cubic crystal structure is distorted and therefore a spontaneous polarisation is established, which means that the polar axes of the crystallites are orientated randomly. This spontaneous polarisation gives rise to a spontaneous deformation which introduces local stress in the crystal. In order to reduce this stress, the polar axes arrange themselves to form domains of different orientation. Depending on the crystal system, only distinct angles of orientation between the domains can occur. For tetragonal systems, angles of 90° and 180° are preferred, for rhombohedral systems 71° and 109° and for orthorhombic systems 60° , 90° , 120° and 180° come into consideration [3].

2.2 Standard materials for piezoelectric applications: Barium Titanate and Lead Zirconate Titanate (PZT)

The currently used standard material for piezoelectric applications is lead zirconate titanate (PZT). PZT is a solid solution of lead titanate (PT) and zirconium titanate (ZT). The phase diagram of PZT (see Figure 2) shows a morphotropic phase boundary (MPB) at a composition of PT:ZT of 52:48 at room temperature. An MPB is a phase boundary between two crystal structures at a certain composition of the system. Due to inhomogeneous mixing of the starting materials the MPB is often not a defined line, but covers a compositional range of the ceramic material in which both phases may coexist. The determination of the MPB is therefore not reached on the basis of structural properties, but rather on the basis of the investigation of electrical properties. This is because the piezoelectric properties reach maximum values at the MPB. The MPB of PZT shows little temperature dependence which means that the phase transition occurs

at nearly the same composition even if the temperature is changed. This is important, because in that case the material properties do not change with temperature changes. With the mixed oxide method the homogeneity of the mixing is not very good. With other methods which provide more homogeneous mixing the MPB will become more accurate.

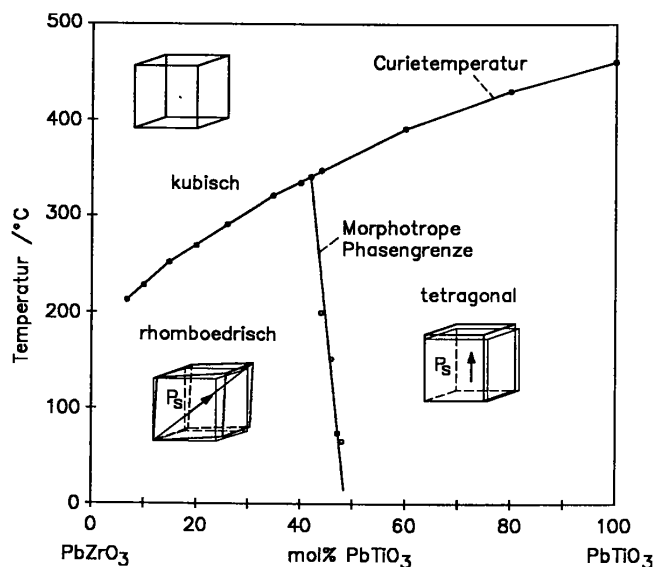


Figure 2: Phase diagram of the system PZT

PZT crystallizes in a perovskite crystal structure which can be distorted in different ways, depending on the temperature. According to the phase diagram of PZT the crystal structure at room temperature is either rhombohedral or tetragonal, depending on the composition. At the Curie temperature a phase transition takes place which results in a cubic crystal structure. As the cubic structure features an inversion center, the material does not show piezoelectric properties beyond this temperature. The phase diagram also shows that PZT is ferroelectric in a wide temperature range, which is important for many applications.

Barium titanate (BT) is another material which shows piezoelectric behaviour. It does not contain lead, but is not as suitable for applications as PZT because of several disadvantages: its Curie temperature is rather low ($T_C = 110^\circ\text{C}$) and its coupling constant k_{33} is just 0.36 while that of PZT ranges between 0.5 and 0.7 [3]. Therefore, the en-

ergy conversion of barium titanate is much less effective than that of PZT (just 13% instead of 50% for PZT [3]). Like PZT, barium titanate crystallizes in a perovskite crystal structure. Beyond T_C it is cubic, at room temperature it is tetragonal. There is a phase transition to an orthorhombic lattice at 5°C . A rhombohedral modification exists at low temperatures with a phase transition temperature of -70°C . The phase diagram of barium titanate is shown in Figure 3.

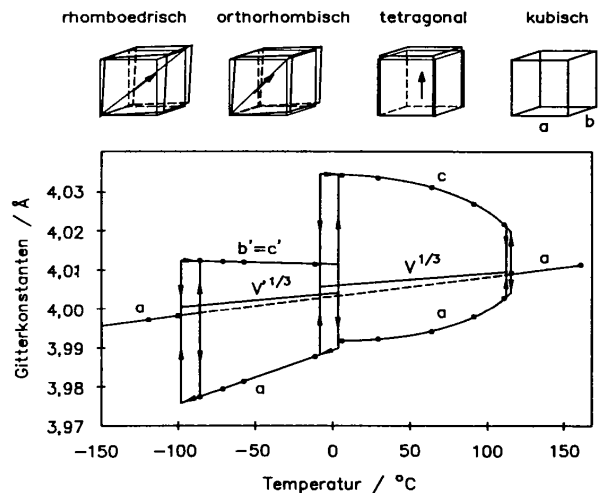


Figure 3: Phase diagram of the system BT

Transmission electron microscope investigations showed the domain structures of the standard piezoelectric materials PZT and barium titanate (compare [5], [6]).

Ceramics in technical applications are always modified to achieve certain properties. A modification can be achieved by means of doping. In PZT, doping with a donor substance (e.g. La^{3+} instead of Pb^{2+} on A-sites), for example, causes higher domain wall mobility and therefore better properties concerning the dielectric constant, the elastic compliance and the coupling coefficient and reduces the coercive field. Doping with cations of higher valency can also prohibit abnormal grain growth.

2.3 The way to lead-free, piezoelectric materials

This chapter is based on the publications [7], [8], [9] and [10].

When searching for new, lead-free materials it is important to have knowledge about the relationship between the nature of a material and its ferroelectric behaviour and to know how to maximize the piezoelectric parameters of these materials. The latter is related to the existence of a morphotropic phase boundary, because the electrical properties reach a maximum at this composition. As mentioned, PZT features such an MPB. On the other hand, the existence of a polymorphous phase boundary is of importance, too. A polymorphous phase transition takes place as a function of temperature. The methods to find new, lead-free ferroelectric materials are not only based on experiments, but also on the establishment of models in order to be able to calculate and simulate the properties of different materials. With ab-initio methods, for example, it is possible to solve chemical questions on the basis of quantum mechanics.

It has been found out that the hybridization and hence a covalent bond character play a decisive role in the question of whether a material does show ferroelectric behaviour or not. The 3d orbitals of titanium or lead and the 2p orbitals of oxygen, for example, are hybridised, while the interaction between barium and oxygen is purely ionic. On the other hand, the off-centering of an A-site ion like lithium can also give rise to ferroelectricity.

In order to be able to compete against lead, a chemical element has to feature a high polarisability as well as a lone electron pair in an outer electron shell. A high polarisability is provided by elements with a large ionic radius and a large number of electrons. Bismuth meets both demands. The toxicity and the costs of the starting materials are also important considerations. Accounting for these parameters and according to calculations, bismuth is believed to be the only element which has the potential to replace lead in piezoelectric applications.

2.4 Types of lead-free piezoelectric ceramics

This chapter is based on publication [7].

2.4.1 Classification due to crystal structures

Four different types of crystal structures have been investigated so far:

- Perovskites
- Bismuth layer structures
- Non-perovskite structures (e.g. LiNbO_3)
- Tungsten-bronze-structures

The **perovskite structure** is represented by the chemical formula ABO_3 . The perovskite structure is a face centered cubic unit cell in which the corners or A-sites are occupied by a large cation whereas the body centered position or B-site is occupied by a small cation. The oxygen ions form octahedrons around the B-site cation, which are corner linked among each other (see Figure 4).

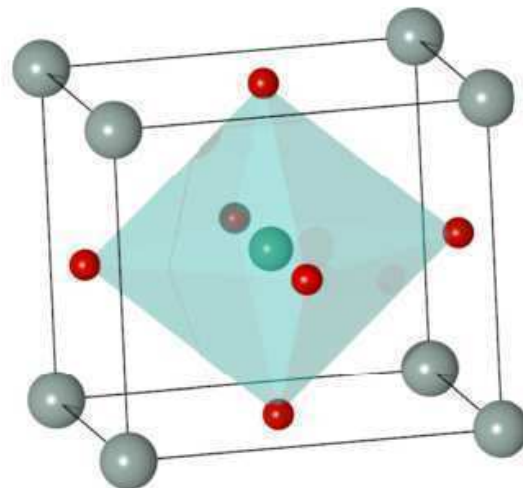


Figure 4: Unit cell of the perovskite structure

The cubic structure features an inversion center and hence does not show piezoelectricity. There are, however, several possibilities of a distortion of the cubic structure which occur in dependence of temperature.

- tetragonal (along the direction 100)
- orthorhombic (along the direction 110)
- rhombohedral (along the direction 111)
- monoclinic or triclinic (along arbitrary directions)

The Goldschmidt tolerance factor t (Equation 3) gives a rough estimation whether a combination of certain ions will form a perovskite lattice or not. In the equation, R_A , R_B and R_O correspond to the radii of the A-site, B-site and oxygen ion, respectively. According to Goldschmidt, the perovskite structure is stable in a range between $0.9 < t < 1.1$. [11]

$$t = \frac{(R_A + R_O)}{\sqrt{2}(R_B + R_O)} \quad (3)$$

Bismuth-Layer-Structures are another type of lead-free ferroelectric structures. The chemical formula is represented by $\text{Bi}_2\text{A}_{x-1}\text{B}_x\text{O}_{3x+3}$. As shown in Figure 5, the structure is characterised by alternating layers of perovskite and $(\text{Bi}_2\text{O}_2)^{2+}$.

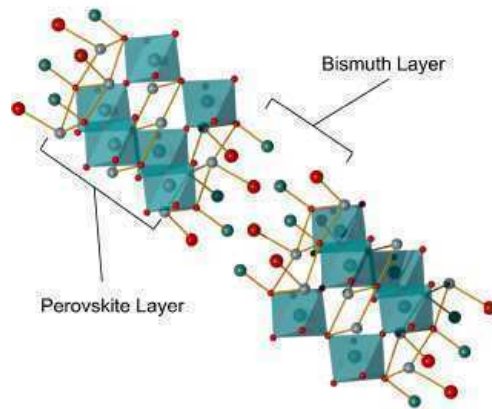


Figure 5: Bismuth-Layer-Structure

The number of unit cells in the perovskite layer can vary and is indicated by the variable x in the chemical formula. An example for a bismuth layer structure is $\text{Bi}_4\text{Ti}_3\text{O}_{12}$ where $x = 3$. The paraelectric phase beyond T_C is tetragonal. Therefore, there are fewer possibilities of lattice distortion below T_C compared to a perovskite structure.

Although LiNbO_3 is represented by the chemical formula ABO_3 , which is typical for perovskites, its tolerance factor which is around 0.5 is too small for crystallization in the perovskite structure. In the LiNbO_3 structure oxygen forms corner linked octahedrons around the niobium ions while lithium occupies the sites between the octahedrons (see Figure 6).

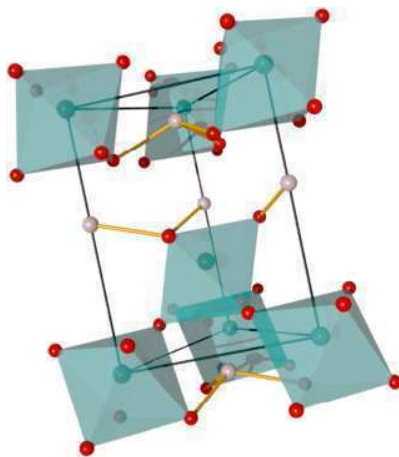


Figure 6: The structure of lithium niobate

Tungsten-bronze-structure. Some compounds which crystallize in the tungsten-bronze-structure also show ferroelectric behaviour. They are represented by the chemical formula $A_x\text{B}_2\text{O}_6$. The B-sites are surrounded by oxygen octahedrons and can be occupied by the elements Ti, Nb, Ta and W. Each unit cell provides 2 A-sites, 4 B-sites and 4 C-sites. The C-sites are very small, hence they are rarely occupied. Only Li is small enough to occupy a C-site. The paraelectric phase beyond T_C is tetragonal. Hence, compared to the perovskite structure, there are fewer possibilities of lattice distortion for this structure, too.

2.4.2 Classification due to the chemical composition

Concerning lead-free materials, the following types have been investigated so far:

- Potassium Sodium Niobate (KNN) - a solid solution of potassium niobate (KN) and sodium niobate (NN)
- Bismuth Sodium Titanate (BNT) and Bismuth Potassium Titanate (BKT) - solid solutions of bismuth titanate and sodium titanate or potassium titanate
- Barium Titanate (BT) (see Chapter 2.2)

In order to obtain a material which shows ferroelectricity and hence also piezoelectricity, at least one of the components has to be ferroelectric. Concerning KNN, for example, KN is ferroelectric while NN is not. The following paragraph will describe the mentioned material types more detailed.

KNN. The end components of KNN, potassium niobate and sodium niobate are both orthorhombic at room temperature. KN is ferroelectric and shows the same phase transitions as BT which are, however, shifted to higher temperatures (compare Figure 3). The coupling coefficient in a certain direction reaches the values for PZT. That is, however, the only important feature of KN as a piezoelectric material. NN is antiferroelectric and hence not piezoelectric.

The phase diagram of KNN is complex and shows several phase transitions and MPBs. One of them is located at 47.5% KN and is vertical until the Curie temperature is reached (see Figure 7). For nearly all compositions, there is a phase transition between different ferroelectric phases at 200°C. The Curie temperature of KNN is situated at 400°C, which is rather high for a ferroelectric ceramic. Also the last statement applies to nearly all compositions.

The preparation of polycrystalline KNN according to the mixed oxide route is difficult. Inhomogeneities of the local chemical composition and volatility of alkali oxides are just

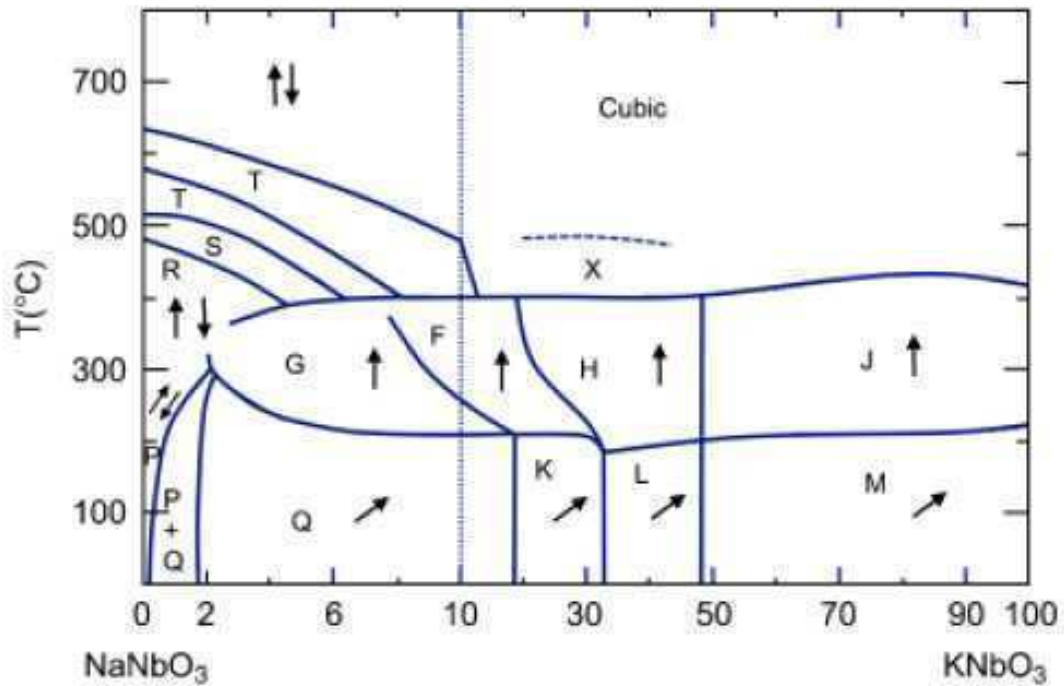


Figure 7: Phase diagram of the binary system KNN [13]

two of the problems. Furthermore, there are difficulties concerning densification during sintering as well as high temperature stability of the perovskite structure. Therefore, KNN was not considered for applications for a long time. Since the call for lead-free alternatives to PZT, however, there is effort to solve these problems.

Chemical modifications have been carried out by means of doping with Ta, Li and Sb so far (compare [12]). Tantalum prohibits abnormal grain growth, but decreases the Curie temperature and the temperature of the phase transition between the orthorhombic and the tetragonal phase (O-T-transition). The latter is also the result of doping with lithium, although lithium raises T_C . The densification during sintering is higher due to doping with lithium. The addition of barium titanate decreases the O-T-transition to room temperature.

BNT and BKT. The systems BNT and BKT are not suitable for piezoelectric application due to their properties. Binary systems with BT as well as binary systems of

BNT and BKT, however, show enhanced properties.

BNT crystallizes in a perovskite lattice and shows ferroelectric behaviour at room temperature. There are phase transitions between 200°C and 320°C (transition between a rhombohedral and a tetragonal structure) and at 520°C (transition between a tetragonal and a cubic structure) [14, 15]. The phase diagram of BNT shows an MPB, which is, in contrast to PZT, curved. This is one disadvantage compared to PZT, because a curved MPB causes a temperature dependence of material properties. Furthermore, sintering and poling is difficult with BNT. The sintering behaviour, however, can be enhanced with excess of bismuth.

BKT crystallizes in a tetragonal lattice and shows a Curie temperature as high as 370°C as well as a phase transition at 300°C. Similar to BNT, both poling and sintering of BKT are difficult.

Binary systems: BNT-BT, BKT-BT, BNT-BKT. Among the bismuth based compounds the binary systems BNT-BT, BKT-BT as well as BNT-BKT have been investigated. BNT-BT shows an MPB at 6 mole% BT, which is, however, curved (see Figure 8). Unlike BNT and BKT, there are no difficulties with those systems concerning the sintering process. The ferroelectric properties of BKT-BT, however, make this system unsuitable for applications. The crystal structure of $\text{BNT}_{1-x}\text{-BKT}_x$ changes from rhombohedral to tetragonal at about $x=0.25$ (compare [16]). A comprehensive study of the local distortion of the structure is given in [17].

Figure 8 depicts the phase diagram of BNT-BT. There is an MPB at 6 mole % of BT. At this composition, a piezoelectric coefficient d_{33} of 125 pC/N, a relative permittivity $\epsilon_{r(33)}$ of 580, a coupling coefficient k_{33} of 55 and a loss factor $\tan \delta$ of 1.3% were found. Samples prepared by a citrate method showed even higher piezoelectric coefficients d_{33} of 180 pC/N (compare [18]). The disadvantages of this compound are based on a curved MPB, a rather low Curie temperature of $T_C = 288^\circ\text{C}$ as well as a very low depolarisation temperature T_d of 130°C. There are no disadvantages concerning the sintering behaviour of BNT-BT. Sintering is carried out at 1100°C - 1200°C. Modifications such as doping have not brought about significant improvements of the properties of BNT-BT. BKT-BT, in contrast to BNT-BT, does not show satisfying piezoelectric properties.

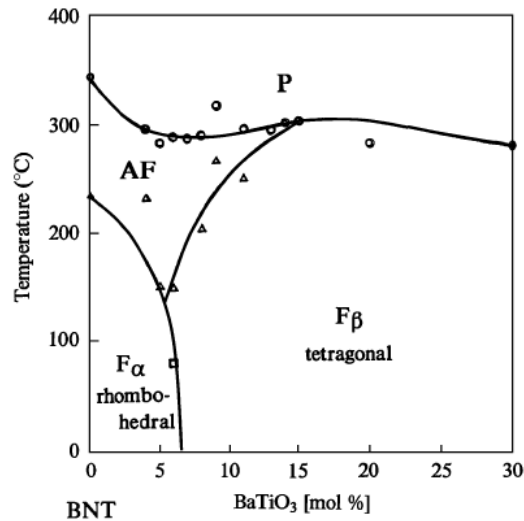


Figure 8: Phase diagram of the system BNT-BT [19]

As far as the preparation of bismuth based materials is concerned, enhanced properties of polycrystalline samples could be reached through texturing. The problems of densification could be solved with the method of hot pressing, but this process is too expensive for large-scale applications. Single crystals can be prepared by several methods, the Czochralski method amongst others. Depending on the method, decreased but also strongly enhanced properties could be reached in comparison to polycrystalline samples. The preparation of single crystals is, however, more expensive than that of polycrystalline material.

In order to solve the problems of the preparation and properties of bismuth based materials, doping with different substances has been examined. Modifications aim at a reduction of the sintering temperature, full poling and enhanced electrochemical properties as well as an increase in Curie temperature. A decrease of the sintering temperature as well as an increase of the density were, for example, reached due to doping with Fe^{3+} ions. The effects of other doping substances such as Li, Mn or Ce, for example, were investigated, but the effects were mostly insignificant and were often accompanied by a decrease of the depolarisation temperature T_d .

3 Methods

This chapter covers the basic principles of transmission electron microscopy and is based on [20], [21], [22], [23] and [24].

3.1 The Transmission Electron Microscope (TEM)

The transmission electron microscope (TEM) consists of an electron source at the top of the column, various electromagnetic lenses and apertures, a specimen stage as well as a viewing screen at the bottom of the column. Concerning image formation using an objective lens, different planes can be defined: the object plane, the lens plane, the back focal plane and the image plane. These planes are schematically shown in Figure 9. The same figure also shows the object distance d_0 and the image distance d_i . Their ratio is defined as the magnification of an image.

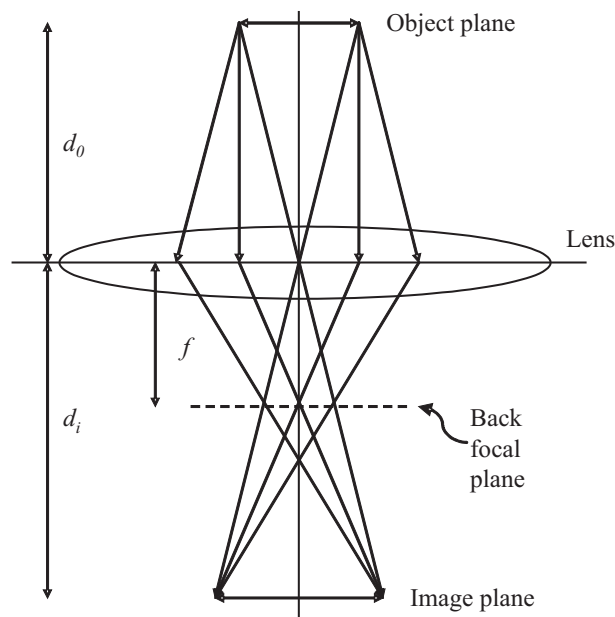


Figure 9: Definition of different planes in a lens system

3.2 The assembly of a TEM

3.2.1 The electron gun

One main component of the electron gun is the source (or cathode) which emits the electrons, either by thermionic or by field emission depending on the type of gun used. In a thermionic source the energy needed to overcome the work function is provided by heating the material in the source. Therefore, either a refractory metal like tungsten or a material with a low working function, like LaB₆, has to be used. A field emission source comprises two anodes. The first one is positively charged with respect to the tip. This so called extraction voltage enables the electrons to overcome the working function and to tunnel out of the tungsten tip. The second anode is responsible for the acceleration of the electrons.

As shown in Figure 10 (a), **thermionic guns** comprise the electron source, a Wehnelt cylinder and an anode plate.

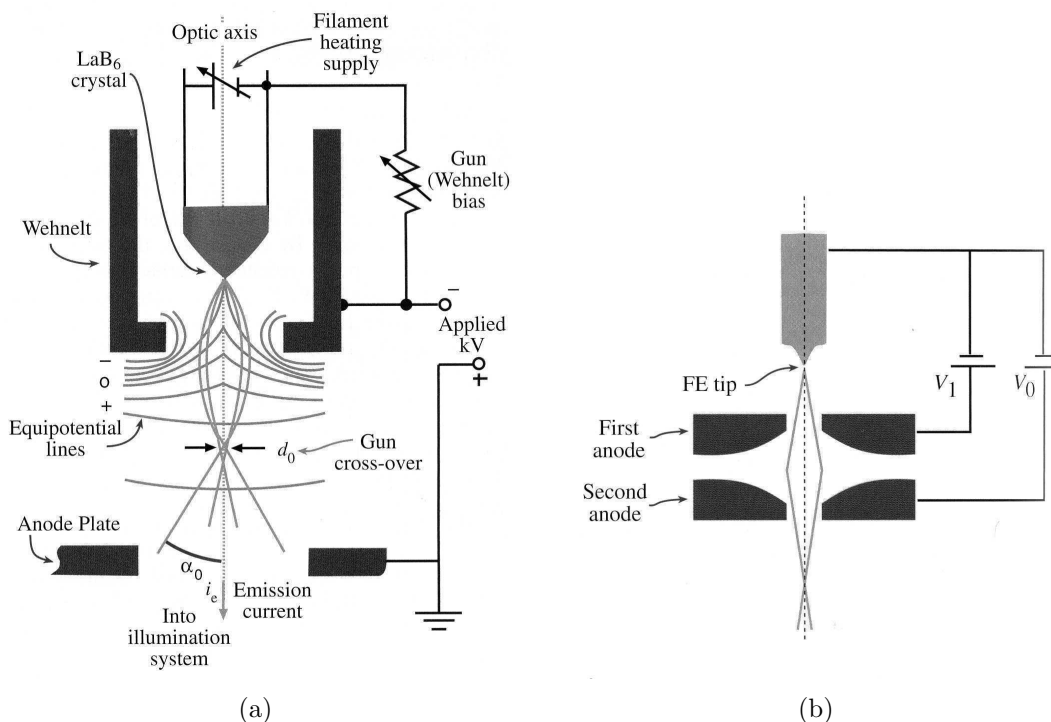


Figure 10: Electron guns: thermionic gun (a) and field emission gun (FEG) (b) [20]

The Wehnelt cylinder acts as a lens and hence focuses the electrons into a point called the gun crossover. Because of a potential between the cathode and the anode the electrons are accelerated towards the illumination system of the TEM. **Field emission guns** (Figure 10(b)) consist of a tip and two anodes. One anode accelerates the electrons and both together act as an electrostatic lens which focuses the electrons in the gun crossover.

3.2.2 The illumination system

Usually, the illumination system consists of two condenser lenses (C1 and C2), one that forms a demagnified image of the gun crossover (C1) and one for adjusting the illumination mode (C2) which can be either **parallel** or **convergent**. Furthermore, condenser apertures of different sizes can be inserted. An aperture decreases the convergence angle of the electron beam and therefore increases the coherence of the beam. The principle of operation of an aperture is shown in Figure 11.

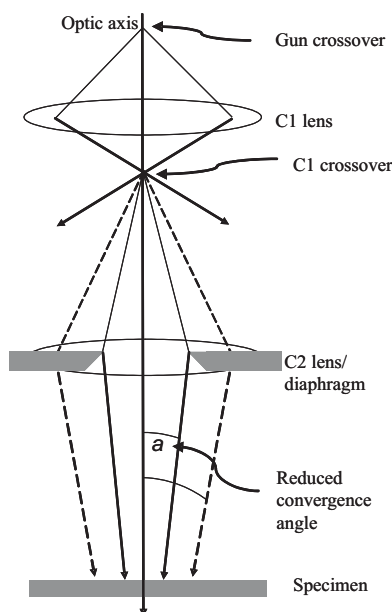


Figure 11: Restriction of the convergence angle of the beam by an aperture [20]

In order to generate a parallel beam, the C2 lens is weakened to underfocus the electron beam while in the convergent illumination mode the beam is focused on the specimen.

The two operation modes are shown in Figure 12.

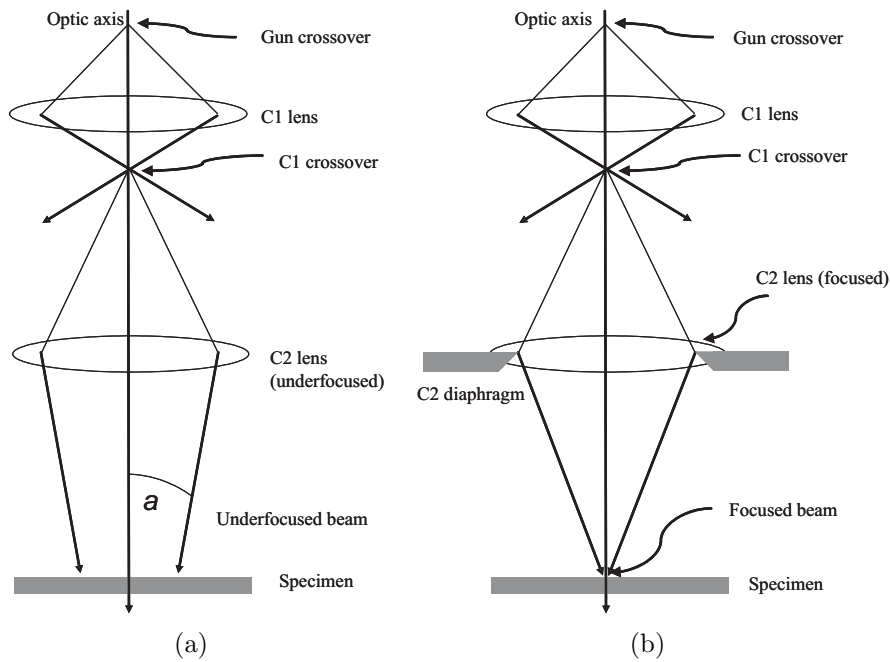


Figure 12: The TEM illumination system: (a) Parallel beam mode and (b) convergent beam mode [20]

3.2.3 The imaging system

The imaging system consists of the objective lens, which is the most important lens in a TEM, an objective aperture and at least two other lenses, the intermediate lens and the projector lens.

While traversing through the thin parts of the specimen, the electrons are scattered by the specimen through particular angles. After the specimen the electrons go through the objective lens which generates the first image of the specimen. This image acts as the object plane for the next lens which creates an image that is further magnified by the intermediate lens. The intermediate lens itself produces another image that acts as the object plane for the projector lens. The final image can be observed on the viewing screen or, alternatively, with a CCD camera. This procedure takes place when the TEM is operated in image mode. A TEM can also work in diffraction mode. In the diffraction mode, the back focal plane of the objective lens acts as the object plane

3 Methods

for the intermediate lens. The rest is similar to the image mode. Finally, a diffraction pattern (DP) can be observed on the viewing screen. The two operation modes are shown in Figure 13.

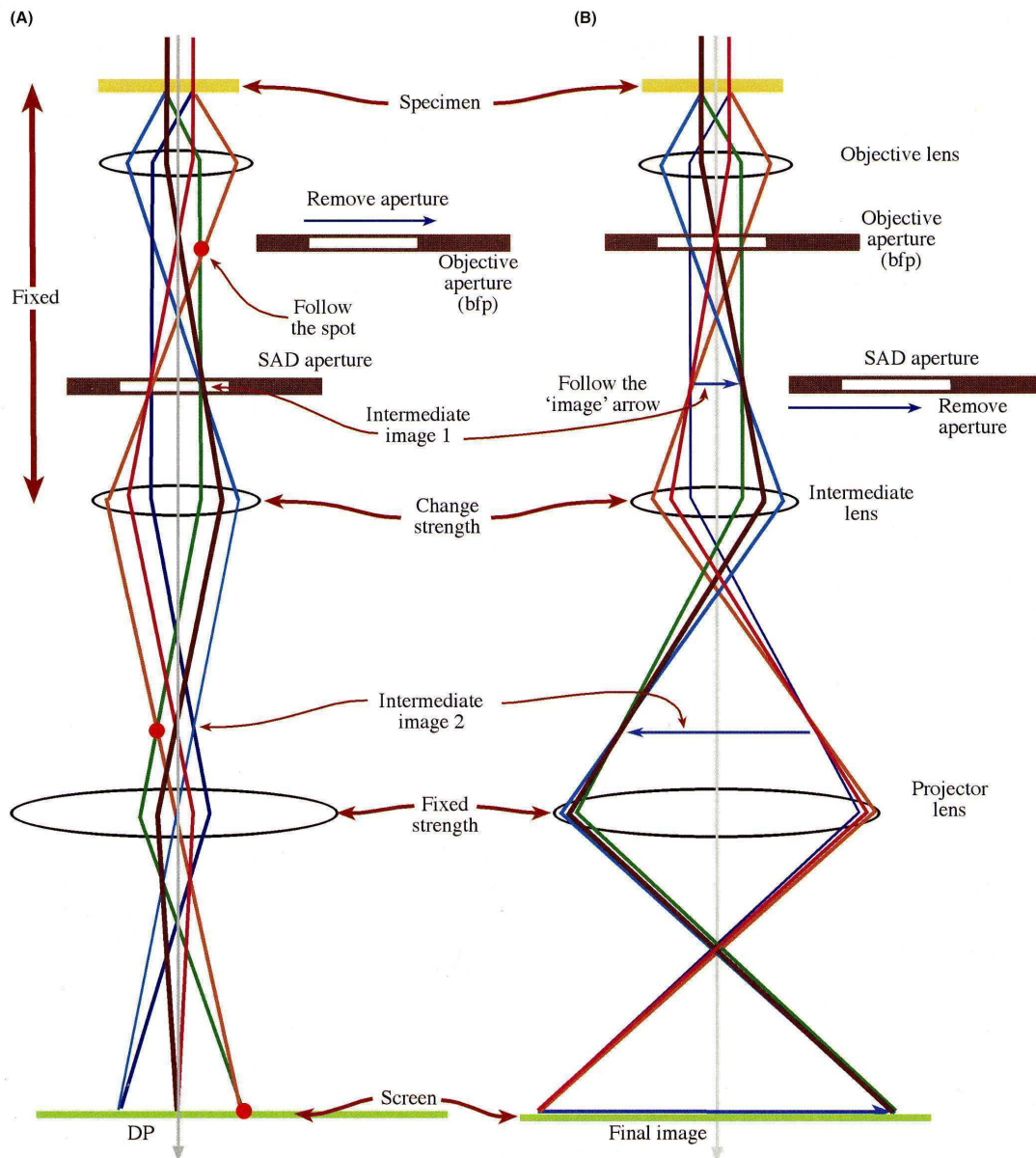


Figure 13: The imaging system in a TEM: (a) diffraction mode (b) imaging mode [20]

3.3 Operation modes

3.3.1 Electron Diffraction

Crystalline materials like the materials investigated in this work are made up of a periodical repetition of atoms referred to as the (real) lattice. In such a lattice different lattice planes can be defined. If the electron beam traverses a crystalline specimen, it is scattered by the atoms in the specimen. If the Bragg condition (see Equation 4) is fulfilled for a set of parallel planes, a bright spot can be observed on the viewing screen.

$$n\lambda = 2d \cdot \sin\theta \quad (4)$$

To fulfill the Bragg condition for different sets of planes the specimen has to be tilted. A diffraction pattern is shown in Figure 14.

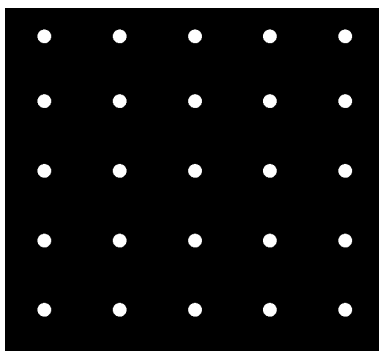


Figure 14: Diffraction pattern

Electron diffraction can be achieved in two ways in the TEM, by means of selected area electron diffraction (SAED) or convergent beam electron diffraction (CBED). To obtain SAED patterns, the specimen is illuminated by a parallel beam and an SAED aperture is inserted to restrict the specimen area that is contributing to the diffraction pattern. To obtain CBED patterns, the electron beam is focused on the specimen to form a small convergent probe. Both SAED and CBED diffraction patterns are shown in Figure 15.

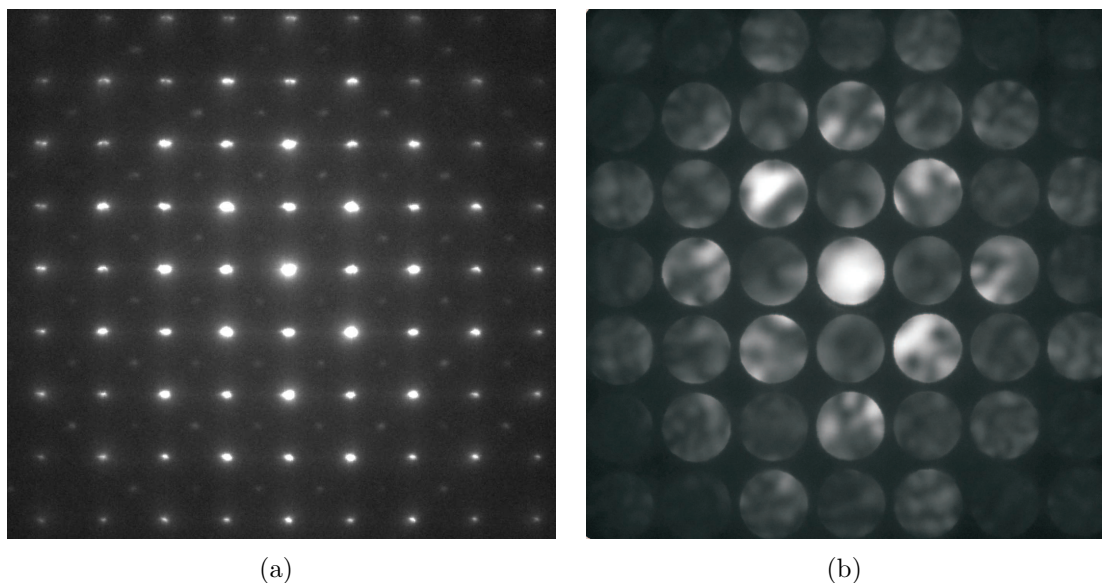


Figure 15: Electron diffraction: (a) SAED (b) CBED

By means of CBED, features smaller than 100 nm such as crystal defects, particles or second phase precipitates can be examined, which is not possible using SAED. Additionally, CBED provides information on point group and space group of the sample due to so called HOLZ (high order Laue zone) lines. For more information on this see [20]. However, this technique was not used in this work, because no HOLZ lines were visible in the CBED patterns of the investigated samples.

3.3.2 Imaging Mode

Bright field and dark field images. In an electron microscope one can create either bright field or dark field images. A bright field image (BF) is generated by electrons of the direct (or primary) beam only. A dark field image (DF) is generated only by those electrons which had been scattered in one particular direction (e.g. one spot in the diffraction pattern). To obtain a BF image, the objective aperture has to be centered around the primary beam. To create a DF image any diffracted spot is selected with the objective aperture by tilting the incident beam (see Figure 16).

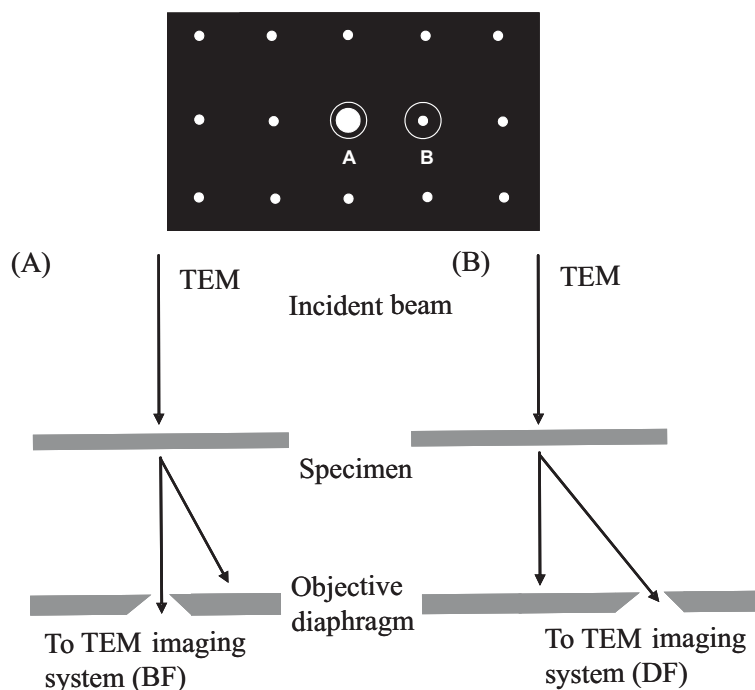


Figure 16: Selection of (a) the direct beam or (b) a scattered beam to produce a BF or a DF image, respectively [20].

Image contrast. Contrast is defined as the difference in intensity of two adjacent areas. If an electron is scattered it can change its amplitude or the phase. Hence, amplitude contrast and phase contrast are the two types of contrast in a TEM. There are two types of amplitude contrast - mass-thickness contrast and diffraction contrast. **Mass-thickness contrast** means that the electrons that go either through thicker areas in the specimen or through areas with a higher average atomic number Z and hence higher mass, have to interact with more material and are therefore scattered more strongly. In a bright field image these regions will appear darker than thinner or lower-mass regions, in a dark field image the opposite will be true. **Diffraction contrast** is a sort of amplitude contrast where the electrons are scattered through particular angles. As already mentioned, either the direct beam spot or the spot of any diffracted beam can be selected with the objective aperture to gain BF or DF images. Then, regions in which the Bragg condition is fulfilled will appear bright and others will appear dark in a BF image and vice versa in a DF image. Therefore, regions with different crystal orientation can be visualized with diffraction contrast.

Phase contrast arises from the interference of two or more scattered electrons. The resulting images are called high resolution images and the technique is called high resolution TEM (HRTEM). In this way, lattice defects such as voids or dislocations can be detected with atomic resolution.

3.4 Chemical analysis with energy dispersive x-ray spectroscopy (EDXS) and electron energy loss spectrometry (EELS)

The interaction of the electron beam with the atoms of the sample can be either elastic or inelastic. An elastic interaction only changes the direction of the primary electron while an inelastic interaction additionally changes the electron energy. The primary electrons are subject to energy loss mainly due to four interaction processes: phonon excitations ($\Delta E=0.02$ eV), interband and intraband transitions ($\Delta E=2-20$ eV), excitation of collective vibrations in the conduction band, so called plasmons ($\Delta E=5-30$ eV) and the ionization of inner shell electrons ($\Delta E=50-3000$ eV). Information on the chemical composition of the sample can be obtained from the detection of either the energy loss of the primary electrons (electron energy loss spectroscopy, EELS) or the characteristic X-ray energy which is released when a specific element is ionized (energy-dispersive X-ray spectrometry, EDXS). In both cases, a spectrum is obtained by measurement over an energy range.

3.4.1 The EEL spectrum

The EEL spectrum consists of an exponentially decreasing background and characteristic ionization edges. The background consists of energy losses from plasmons and plural scattering events as well as single scattering contributions from the tails of the preceding ionization edges. The characteristic ionization edges are the result of interactions between the primary electrons with the electronic shell of a specific element. The position of the ionization edges in the spectrum is hence characteristic for specific elements. The EEL spectrum is split up into a low-loss (about 0-50 eV) and a high-loss regime

(>50 eV). The low-loss regime comprises the zero-loss peak (electrons that have not suffered inelastic scattering) and the plasmon peak. The high-loss regime comprises the ionization edges. The position of the ionization edge yields qualitative information about the type of element, the intensity above background yields quantitative information.

In the transmission electron microscope, the EELS detection unit is positioned either after the viewing screen or between the specimen and the viewing screen. The two systems are referred to as post-column filters and in-column filters, respectively. The electrons which were scattered while traversing the sample are first selected by an entrance aperture. A magnetic prism acts as the spectrometer by deflecting the electrons through angles higher than 90° using a magnetic field. The more energy an electron has lost, the further it is deflected. Thus, a spectrum of electron intensity versus energy loss is created.

With EELS, all elements can be detected with the exception of the elements with a lower atomic number than lithium.

3.4.2 The EDX spectrum

The EDX spectrum consists of a background of bremsstrahlung and element characteristic peaks. The bremsstrahlung arises from the interaction of the primary electrons with the nuclei of the atoms while the characteristic peaks result from ionizations of inner shell electrons. When an inner shell electron is excited by a primary electron, the resulting vacancy is filled by an electron of a higher electron shell. The difference in energy between those two states is released as an X-ray photon of a characteristic energy for each element. The generated X-rays are collected with a semiconducting detector which can be either an HPGGe (high-purity Germanium) or a Si(Li) detector. The position of the characteristic peaks yields information on the type of element, the background corrected intensity is a measure for the concentration of the element.

The detector window restricts the number of elements which can be detected due to absorption at low X-ray energies. There are several types of windows: Beryllium win-

dows with a thickness of about 7 μm , ultra thin windows (UTW) and atmospheric thin windows (ATW). UTW and ATW use a polymer film of about 300 nm thickness. Also, windowless detectors are used sometimes. Beryllium windows allow for detection of elements with atomic numbers of sodium ($Z=11$) or higher, while with UTW and ATW chemical elements such as boron ($Z=5$), carbon, oxygen and nitrogen are detected. In special systems, windowless detectors are used which allow for the detection of even beryllium ($Z=4$).

4 Specimen

This work focuses on the lead free ferroelectric group bismuth-alkali-titanates. Two binary systems were investigated:

1. Bismuth Sodium Titanate - Barium Titanate
 $\text{Bi}_{0.5}\text{Na}_{0.5}\text{TiO}_3\text{-BaTiO}_3$ (BNT_{0.94}-BT_{0.06} or BNT-6BT)
2. Bismuth Sodium Titanate - Bismuth Lithium Titanate
 $(\text{Bi}_{0.5}\text{Na}_{0.35}\text{Li}_{0.15})\text{TiO}_3$ (BNT-15BLT)

The composition of BNT-6BT corresponds to the morphotropic phase boundary (MPB).

4.1 Specimen preparation using the mixed oxide method

The ceramic samples have been provided by the *Institute of Chemical Technology of Materials, TU Graz*. They were prepared according to the mixed oxide method using carbonates and oxides as starting materials. Table 2 provides the initial weights of the components.

Table 2: Amount of starting materials for the preparation of BNT-6BT and BNT-15BLT according to the mixed oxide method

	Mass of component [g]				
	Bi_2O_3	Na_2CO_3	TiO_2	BaCO_3	Li_2CO_3
BNT-6BT	256.885	58.432	187.363	27.777	-
BNT-15BLT	139.047	22.140	95.331	-	0.6615

The powders were suspended in 30 ml of ethanol and ground in a ball mill with the aid of 150 g grinding balls with a diameter of 5 mm. A grinding beaker made of zirconium dioxide was used. After ball milling the suspension was filtered. The remaining ethanol was evaporated in a rotary evaporator. The powder was dried in a drying chamber and afterwards calcined for 3 hours at a temperature of 850°C. After calcination the powder was milled in a mortar and mixed with 20 wt% of the fluxing agents Bi_2O_3 and alkali

carbonates. Conversion and crystallization were performed in a platinum crucible in a tube furnace following the temperature program shown in Table 3. In order to separate the crystals from the remaining fluxing agent, the compound was boiled in concentrated hydrochloric acid.

Table 3: Temperature program for the preparation of BNT-6BT crystals

temperature range	heating rate [°C/h]	holding time [h]
RT - 1250°C	150	-
1250°C - 1300°C	50	5
1300°C - 800°C	5	-
800°C - RT	100	-

4.2 Specimen preparation for investigation in TEM

Powder preparation. For powder preparation the crystals were crushed and milled in a boron carbide mortar and suspended in ethanol. The suspension was deposited on a copper grid coated with a holey carbon film. After the ethanol had evaporated, the specimen was ready for investigation.

Ion milling specimen preparation. Before preparation, the crystals had an edge length of a few millimeters. These crystals were first ground with a diamond grinding paste of 15 μm grain size to a thickness of 550 μm and then cut into slices of 1.7 mm thickness with a diamond wire saw (see Figure 17).

After cleaning in acetone in an ultrasonic bath the crystal platelet was embedded in a small alumina tube. The embedding resin was hardened for two hours at 130°C. After hardening the tube was cut into slices of 0.5 mm thickness and ground to a thickness of 150 μm with a diamond grinding paste of the same grain size as before. Afterwards, the specimen was polished on one side with diamond paste with a grain size of 6 μm for 2 minutes and with a grain size of 250 nm for 3 minutes. After polishing, the specimen was dimple ground on the non-polished side to a thickness of about 19 μm in the center of the sample and subsequently polished with diamond paste of 6 μm and 0.25 μm on this side, too. As a last step, the specimen was ion milled with argon ions of an energy

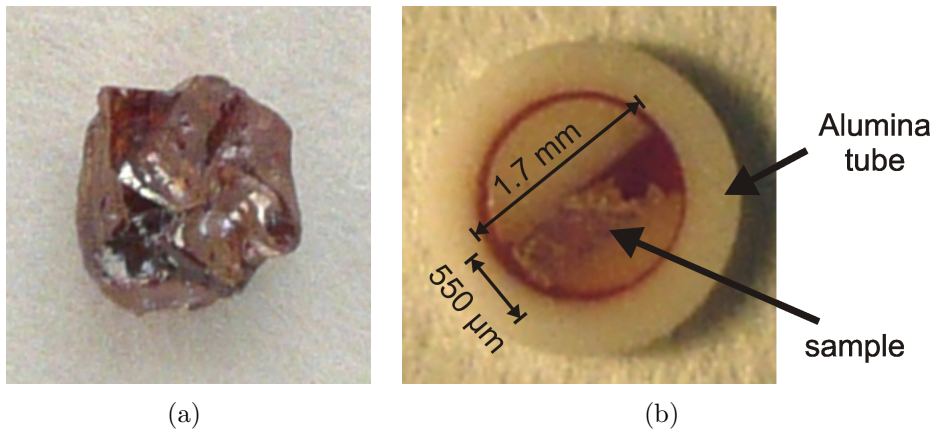


Figure 17: (a) Crystal before preparation. (b) Crystal embedded in an alumina tube.

of 4 kV for 4-5 hours. The samples were hit by the argon ion beam at an angle of 4° regarding the upper surface and an angle of 6° regarding the lower surface.

5 Investigation in TEM

5.1 Transmission Electron Microscopes

For the present work, the transmission electron microscopes FEI Tecnai 12, Philips CM 20 and FEI Tecnai F 20 are used. Their main features and the reasons for the use of different microscopes are described in this chapter. The microscopes are depicted in Figure 18.

5.1.1 FEI Tecnai 12 (T 12)

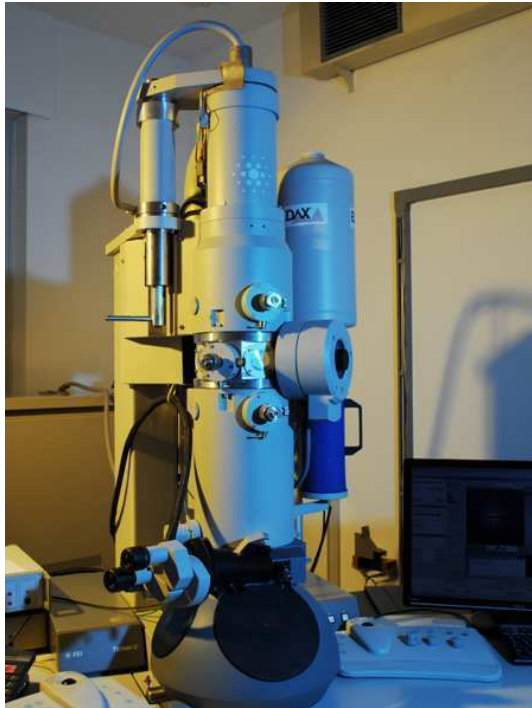
The T 12 was used for standard imaging and electron diffraction. It features a thermionic LaB₆ source and operates at a maximum acceleration voltage of 120 kV. A single tilt specimen holder was used for powder investigations and a rotation tilt specimen holder for single crystal investigations. The T 12 features two cameras for digital image acquisition. The TEM magnification of this microscope ranges from 35x to 700.000x. The TEM point resolution is 0.34 nm, the TEM line resolution is 0.20 nm. Although the T 12 features an EDXS detector, it is not suitable for chemical analysis at the nanoscale because it does not provide STEM operation mode. In STEM mode, a convergent electron beam allows the examination of very small areas. Furthermore, the T 12 does not have any EELS unit.

5.1.2 Philips CM 20

The CM 20 is an analytical microscope and hence allows chemical analysis with EDXS and EELS. It features a post-column Gatan image filter (GIF) including a digital camera. The maximum acceleration voltage at the CM 20 is 200 kV. The electron source is a LaB₆ cathode. The CM 20 provides a TEM point resolution of 0.27 nm and a TEM line resolution of 0.14 nm. The EELS energy resolution is 1.25 eV. The CM 20 has a STEM operation mode.

5.1.3 FEI Tecnai F 20 (TF 20)

The TF 20 features a Schottky Field Emitter and a monochromator as electron source and operates at a maximum acceleration voltage of 200 kV. The TEM magnification ranges from 25x to 2.000.000x. The TEM point resolution is 0.24 nm, the TEM line resolution is 0.10 nm. The TF 20 can be operated in TEM and STEM mode. For the present work, it was used for electron diffraction to detect features with low intensity that could not be detected using the T 12 in a satisfying way. In contrast to the T 12, the TF 20 features a higher maximum acceleration voltage which leads to a higher resolution. Additionally, the TF 20 provides a GIF for energy filtering TEM (EFTEM). The GIF filters inelastically scattered electrons and hence faint reflections become visible. Furthermore, the TF 20 was used for high resolution imaging.



(a)



(b)



(c)

Figure 18: Transmission electron microscopes used for the present work: Tecnai T12 (a), Tecnai F20 (b) and Philips CM20 (c)

5.2 Investigation of $(\text{Bi}_{0.5}, \text{Na}_{0.5})\text{TiO}_3\text{-BaTiO}_3$

The first specimen was $\text{Bi}_{0.5}\text{Na}_{0.5}\text{TiO}_3\text{-BaTiO}_3$ ($\text{BNT}_{0.94}\text{-BT}_{0.06}$ or simply BNT-6BT). BNT-6BT crystallizes in a perovskite structure as shown in Figure 4 in Chapter 2.4.1. The composition of the specimen corresponds to the morphotropic phase boundary (MPB) of BNT-6BT (94% BNT, 6 %BT). As explained in Chapter 2, compositions lower than 6 % barium titanate crystallize in a rhombohedral lattice whereas compositions higher than 6 % barium titanate crystallize in a tetragonal lattice. Often, the MPB is not a well-defined line. Hence, the crystal structure can be either rhombohedral or tetragonal or a mixture of both phases (for the phase diagram see Chapter 2, Figure 8). The specimen was examined at the *Institute of Chemical Technology of Materials (TU GRAZ)* by means of powder X-ray diffraction with a Siemens D 5005 diffractometer with a scintillator counting unit using copper K_α radiation. Rietveld refinement was done with the software *TOPAS*. However, with the results of powder X-ray diffraction it was not possible to distinguish between the two phases that might be present. The X-ray spectra of the crystal systems are very similar and differ only in faint reflections. Therefore, both a tetragonal as well as a rhombohedral model could be established from the measured data. For a rhombohedral distorted lattice the lattice parameters and atom coordinates are shown in Table 4, for a tetragonal distorted lattice see Table 5.

Table 4: Space group, lattice parameters and atom positions for the system BNT-6BT obtained from X-ray analysis with a rhombohedral structure model. (*By courtesy of Denis Orosel, Institute of Chemical Technology of Materials, TU Graz*)

Space group	R3c (161)				
Lattice parameters [Å]	a	5.5126014			
	c	13.5023183			
Atom positions		x	y	z	Occ
	Na	0.00000	0.00000	0.28158	0.47
	Bi	0.00000	0.00000	0.28158	0.47
	Ba	0.00000	0.00000	0.28158	0.06
	Ti	0.00000	0.00000	0.01674	1
	O	0.15760	0.33700	0.07758	1

Due to absorption of the X-rays by heavy elements like bismuth, it was not possible to

Table 5: Space group, lattice parameters and atom positions for the system BNT-6BT obtained from X-ray analysis with a tetragonal structure model. (*By courtesy of Denis Orosel, Institute of Chemical Technology of Materials, TU Graz*)

Space group	P4bm				
Lattice parameters [Å]	a	5.5137143			
	c	3.8956917			
Atom positions		x	y	z	Occ
	Na	0.00000	0.50000	0.55890	0.47
	Bi	0.00000	0.50000	0.55890	0.47
	Ba	0.00000	0.50000	0.55890	0.06
	Ti	0.00000	0.00000	0.00000	1
	O₁	0.00000	0.00000	0.51000	1
	O₂	0.27100	0.22900	0.01500	1

obtain single crystal X-ray diffraction patterns of the present specimen.

In order to be able to determine the crystal structure and its local homogeneity, the specimen was investigated with powder and single crystal transmission electron microscopy. Furthermore, analytical methods were used to examine the local composition. All images and diffraction patterns of the specimen BNT-6BT were acquired using the T 12.

5.2.1 Powder electron diffraction

In order to make a first characterization of the specimen, powder samples were prepared (see Chapter 4.2) and investigated by means of electron diffraction. To get satisfying results, it is necessary to have a large number of small, thin particles on the grid. In this case, a large number of differently orientated particles will result in a ring pattern instead of a single crystal pattern. With this sample, however, some difficulties arising from specimen preparation occurred to obtain a satisfying ring pattern. Despite repeated attempts to prepare a sample with a large number of sufficiently small particles, the number of particles in a particular area was too small and the particles were not small and thin enough, so many of them weren't transparent for the electron beam.

In Figure 19, an example of a powder particle is shown. The depicted particle is about $3 \times 1 \mu\text{m}^2$ in size, but also smaller ones with dimensions of about $0.5 \times 0.2 \mu\text{m}^2$ can be seen.



Figure 19: Particle of the investigated powder sample

Figure 20 (a) shows a powder pattern of BNT-6BT. The reflections are located in the form of concentric rings. The diameter of each ring gives information about the interplanar spacing of the sample. For the analysis of the powder patterns the software Digital Micrograph was used. As a first step, the center of the rings is determined. After that, a line profile starting from the center of the rings outwards is generated. All reflections in a certain distance to the center result in a peak in the line profile shown in Figure 20 (b). Each peak corresponds to a particular interplanar spacing in reciprocal space (nm^{-1}) and hence has to be converted to a distance in real space (nm).

The results were compared with the present X-ray data (see Tables 6 and 7). Analysis of the X-ray data worked for a rhombohedral model as well as for a tetragonal model. Hence, both data sets were compared to the results of powder electron diffraction as shown in the Tables 6 and 7. Unfortunately, the results from electron diffraction are less precise than those from X-ray analysis due to the measuring principle and the analysis of the data (e.g. lens aberrations, focusing errors and measuring inaccuracy concerning analysis). Due to the inaccuracy of the results there is only a rough analogy with the interplanar spacing obtained from X-ray measurements. Therefore, it was not possible to determine the crystal structure by means of powder electron diffraction.

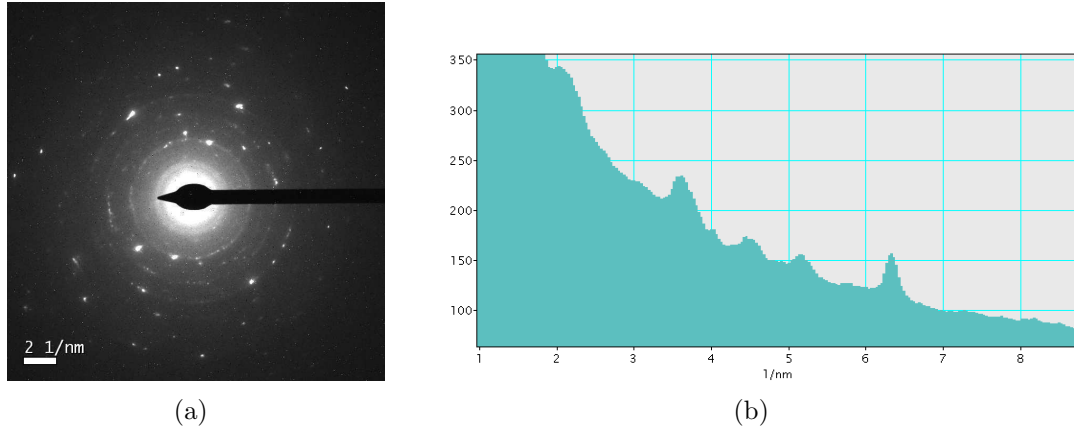


Figure 20: Powder pattern of BNT-6BT (a) and line profile of the powder pattern (b)

Table 6: Results of electron and X-ray powder diffraction for BNT-6BT. The X-ray results are based on a rhombohedral structure model. (*X-ray data: by courtesy of Denis Orosel, Institute of Chemical Technology of Materials, TU Graz*)

electron diffraction		data from X-ray powder diffraction (rhombohedral)						
distance [1/nm]	d-spacing [Å]	d-spacing [Å]	Intensity	h	k	l	Mult.	2θ
-	-	3.8979	1307336.86	0	1	2	6	22.795
3.66	2.74	2.7563	775579.33	-1	2	0	6	32.457
		2.7562	905555.54	-1	1	4	6	32.485
-	-	2.3505	8847.33	-1	2	3	12	38.260
4.50	2.22	2.2505	149415.30	-2	2	2	6	40.032
		2.2504	42300.71	0	0	-6	2	40.034
5.14	1.94	1.9490	1270964.00	0	2	4	6	46.561
5.73	1.75	1.7885	2731.11	-2	3	1	12	51.023
		1.7432	197612.26	-1	3	2	12	52.448
		1.7432	260556.29	-1	2	6	12	52.449
6.34	1.58	1.5914	162818.65	0	3	0	6	57.901
		1.5913	367119.00	-2	3	4	12	57.902
		1.5913	219006.34	0	1	8	6	57.904

Table 7: Results of electron and X-ray powder diffraction for BNT-6BT. The X-ray results are based on a tetragonal structure model. (*X-ray data: by courtesy of Denis Orosel, Institute of Chemical Technology of Materials, TU Graz*)

electron diffraction		data from X-ray powder diffraction (tetragonal)						
distance [1/nm]	d-spacing [Å]	d-spacing [Å]	Intensity	h	k	l	Mult.	2θ
-	-	3.8988	89974.29	1	1	0	4	22.790
		3.8957	51099.20	0	0	1	2	22.809
3.66	2.74	2.7569	60643.03	0	2	0	4	32.450
		2.7558	107641.72	1	1	1	8	32.464
4.50	2.22	2.4658	2829.40	1	2	0	8	36.407
		2.2504	23705.33	0	2	1	8	40.034
		2.0835	2858.81	1	2	1	16	43.396
5.14	1.94	1.9494	104767.76	2	2	0	4	46.551
		1.9478	50227.35	0	0	2	2	46.590
5.73	1.75	1.7436	15290.95	1	3	0	8	52.436
		1.7433	14222.46	2	2	1	8	52.445
		1.7425	21095.92	1	1	2	8	52.472
6.34	1.58	1.5915	47901.33	1	3	1	16	57.897
		1.5908	20821.72	0	2	2	8	57.922

5.2.2 Single crystal electron diffraction

As powder electron diffraction did not yield satisfying results concerning the determination of the crystal structure of the specimen, a single crystal sample was investigated by electron diffraction. All images and diffraction patterns of BNT-6BT were acquired at the T 12.

Figure 21 shows bright field images of an area of about $7 \times 7 \mu\text{m}^2$ of the specimen BNT-6BT. The formation of contrast is due to mass-thickness contrast and bend contours. As expected for a single crystal, no grain boundaries are visible in the images.

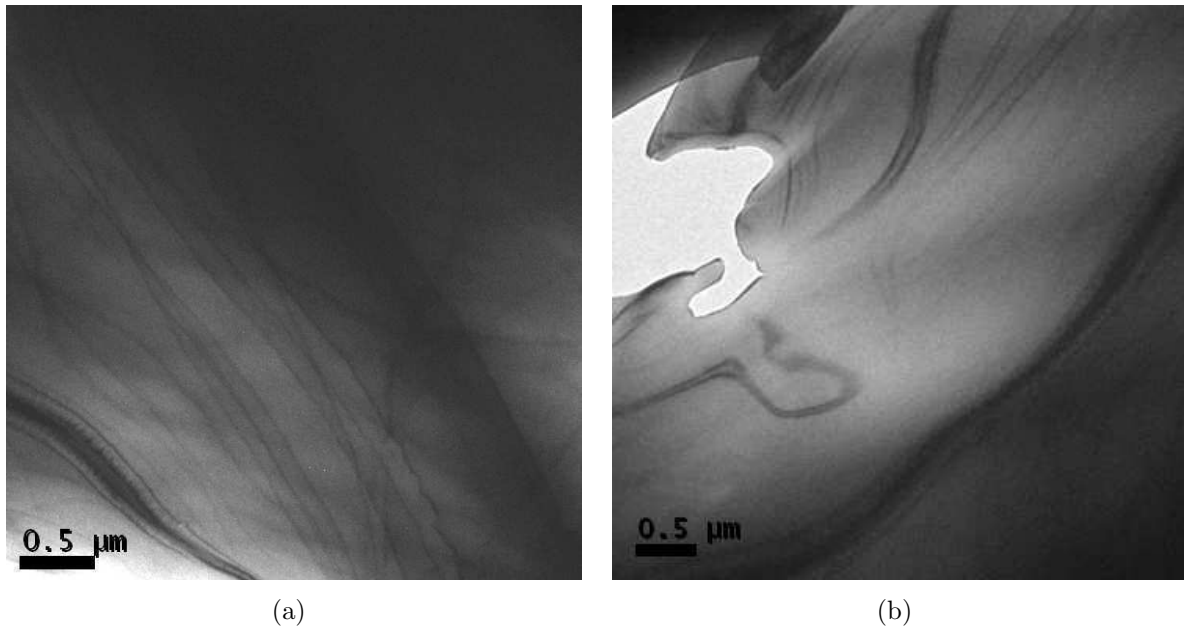


Figure 21: Bright field images of BNT-6BT showing a single crystalline specimen

Figure 22 shows three different diffraction patterns obtained from a sample of BNT-6BT.

In order to determine whether the diffraction patterns referred to a rhombohedral or a tetragonal crystal structure, the diffraction patterns were simulated with the software *Java Electron Microscope Simulator (JEMS)*. Comparison with the acquired diffraction patterns of BNT-6BT revealed that the diffraction pattern shown in Figure 22 (a) corre-

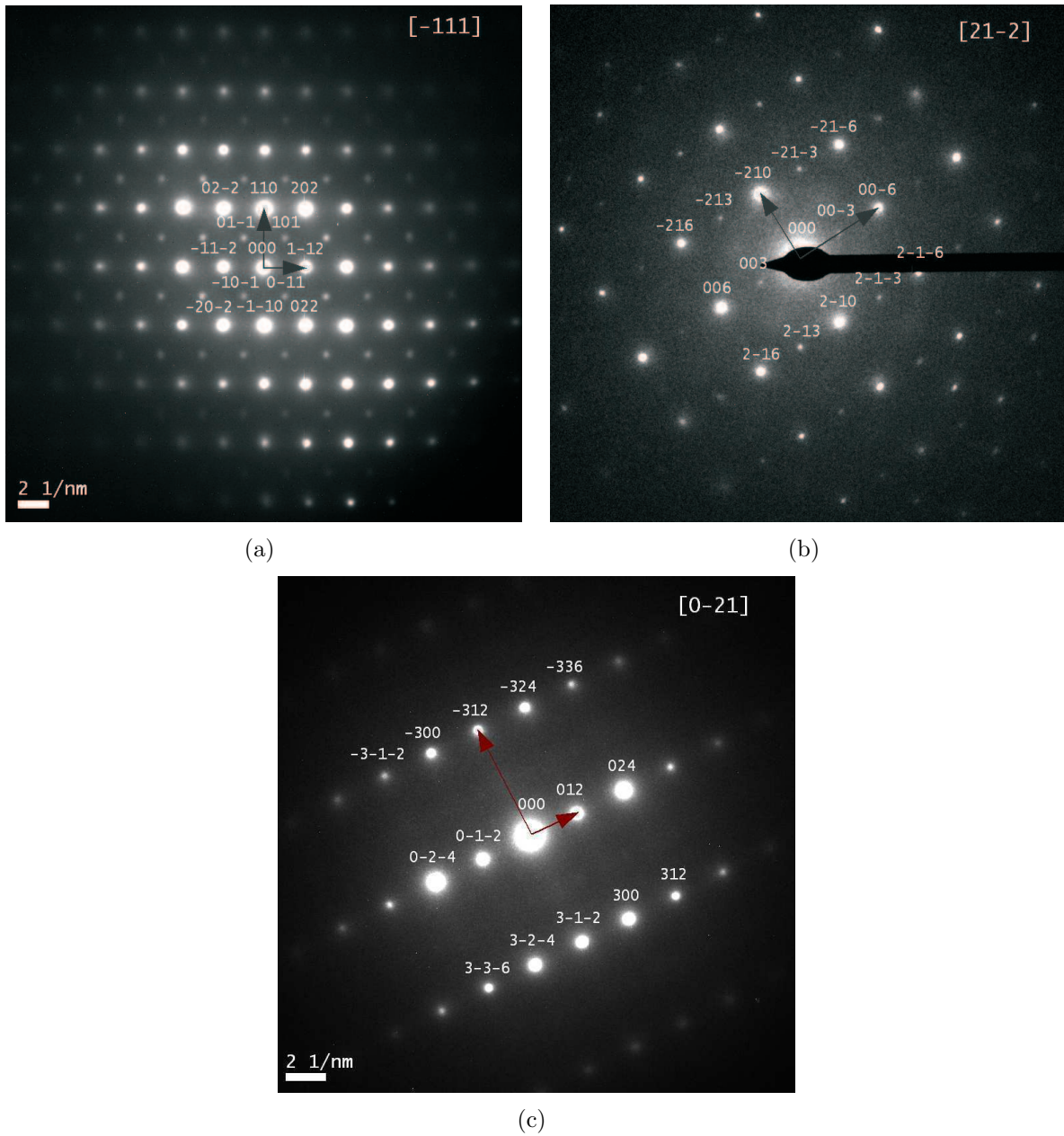


Figure 22: Single crystal diffraction patterns of BNT-6BT in the orientations $[\bar{1}11]$ (a), $[21\bar{2}]$ (b) and $[0\bar{2}1]$ (c) of a rhombohedral lattice

sponded definitely to a rhombohedral lattice due to the faint reflections (see Figure 23).

The diffraction patterns were determined to be down the zone axes $[\bar{1}11]$, $[21\bar{2}]$ and $[0\bar{2}1]$ in Figure 22 (a), (b) and (c), respectively. In order to examine the homogeneity of the

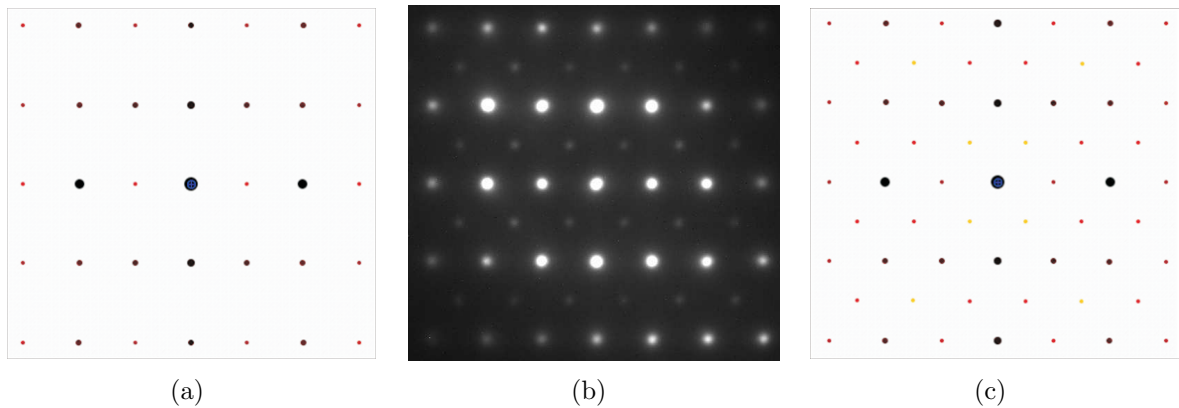


Figure 23: Comparison of a diffraction pattern (b) with a tetragonal (a) and a rhombohedral (c) simulation. Due to the faint reflections, the diffraction pattern is related to a rhombohedral lattice with the zone axis $[\bar{1}11]$.

crystal structure, various parts of the sample were investigated. The diffraction pattern which could be related to a rhombohedral lattice was found in all of the investigated sample regions. Therefore it was concluded that the specimen is made up of a rhombohedral phase with the space group $R\bar{3}c$. The result agrees with the data provided by the Inorganic Crystal Structure Database (ICSD) for BNT-94.5BT [25]. The lattice parameters were calculated using the reflections 110 and $1\bar{1}2$ of the diffraction pattern with the zone axis $[\bar{1}11]$ and are shown in Table 8. The values are compared to those obtained from XRD. The lattice constant a_r obtained from TEM is $3.88 (\pm 0.05) \text{ \AA}$, which is slightly smaller than the value from XRD. By means of XRD, however, a much larger sample volume is examined. The angle α_r is $88.98 (\pm 0.05)^\circ$ and also smaller in TEM.

Table 8: Lattice parameters obtained from TEM diffraction patterns compared with XRD.

BNT-6BT	XRD	TEM
$a_r [\text{\AA}]$	3,90	3,88
$\alpha_r [^\circ]$	90,00	88,98

5.2.3 Chemical analysis of BNT-6BT

Influence of the electron beam on the local composition. As the specimen contains sodium, an alkali metal with a relatively high vapor pressure, the sample may change its local composition during examination under a high energy electron beam. Therefore, experiments have been carried out to check the stability of the composition of the sample under the electron beam. All experiments concerning the chemical analysis were carried out on the CM 20. An area of about $5 \times 2 \mu\text{m}^2$ in size was illuminated using a 200 kV electron beam and investigated by EDX spectroscopy four times consecutively. The spectra 1-4 in Figure 24 were acquired for 60 s, 60 s, 600 s and 1800 s, respectively.

For the analysis of the data the software *NORAN System SIX* was used. The background was corrected using a Gaussian fit to the peaks, a manual adjustment of the background was possible. Each investigated area was illuminated by the electron beam for different periods of time. Therefore, spectra with a good and others with a bad signal-to-noise ratio were acquired. The settings for background subtraction were chosen for a spectrum with high intensity and then adopted to the lower intensity spectra of the same sample region in order to use the same settings for all spectra. After carefully adopting the background the spectra were quantified.

Barium and oxygen could not be quantified due to the following reasons: Oxygen can not be quantified with the method of EDXS because low X-ray energies of light elements such as oxygen are partly absorbed by the sample itself. Therefore, the actual oxygen signal is always lower than the real signal. Barium, though clearly visible in the spectra which were acquired for a long exposure time, was not quantifiable in the spectra of lower intensity because the barium signal mostly vanished due to the noise.

As far as sodium is concerned, two cases are supposable: On the one hand, the local amount of sodium will change immediately after exposure to the electron beam and remain stable afterwards or, on the other hand, it will change so slowly that the effect will be detectable only after long exposure times. In order to check both cases the sample was illuminated for different periods of time. In Figure 24, the at% concentration ratios of sodium to titanium as well as bismuth to titanium are depicted for the four

acquired spectra (measurement numbers 1-4). Comprising the errors, both ratios, Na:Ti and Bi:Ti, show stability under the electron beam. The errors for the measurement numbers 1 and 2 are larger than the errors for 3 and 4 because of the different periods for acquirement.

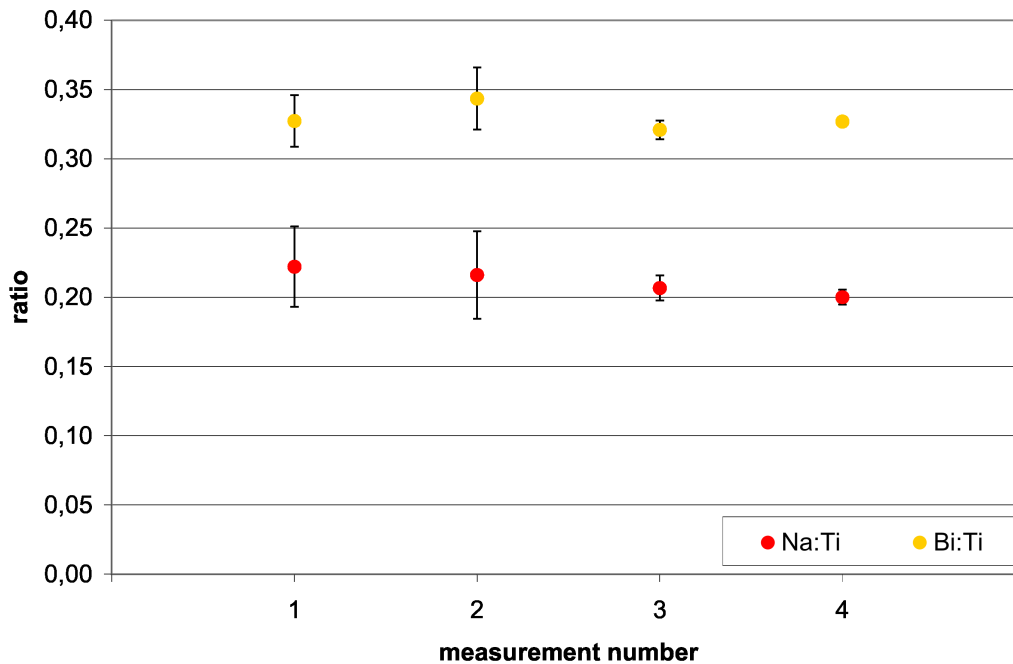


Figure 24: Investigation of the compositional stability of BNT-6BT in the electron beam

The measurement error was calculated according to the method of the highest and the lowest ratio. As shown, the differences in concentration range within the error bars. Thus, the local sample composition seems to remain unaffected by the electron beam.

Investigation of the local spatial composition. As the experiments have shown, the sample does not change its local composition when exposed to the electron beam. Hence, further experiments concerning the homogeneity of the spatial composition could be carried out. A spectrum image (SI) was acquired using both EELS and EDXS. The method of SI combines imaging and spectrum acquisition of the same sample area.

As shown in Figure 25 (a), an area of 18 x 6 pixels, i.e. 108 measurement points, was investigated with EEL and EDX spectra imaging. The area is about 2 x 1 μm^2 in size. Figure 25 (b) shows an example for an EEL and an EDX spectrum.

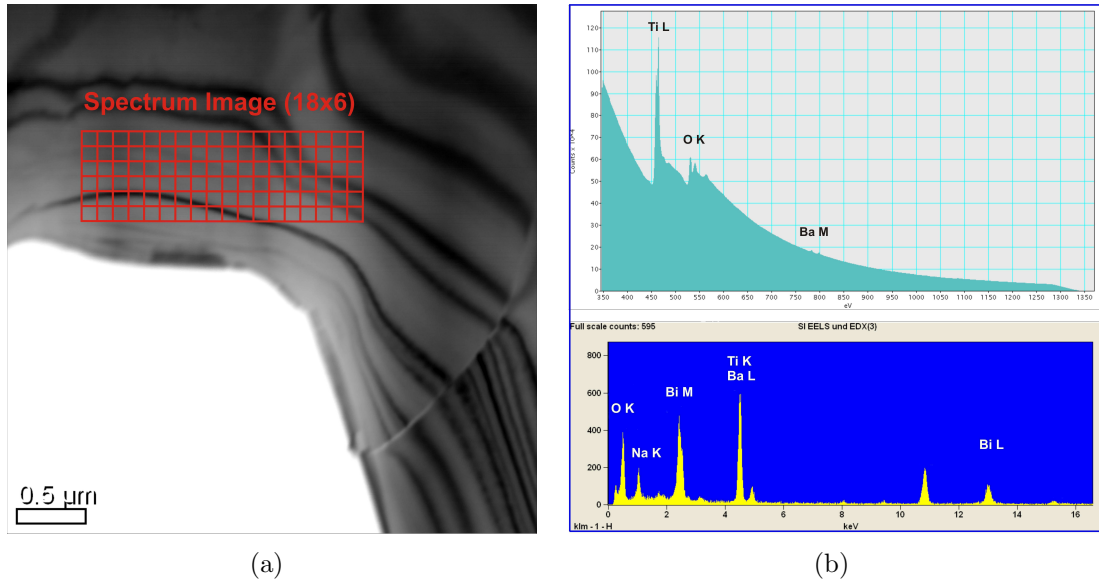


Figure 25: (a) Spectrum Image of a sample of BNT-6BT: 18 x 6 measuring points in an area of 2 x 1 μm^2 . (b) Example EEL and EDX spectra.

The EEL spectra were collected at an acceleration voltage of 200 kV in an energy range from 350 to 1300 eV. The EDX spectra were collected in an energy range from 0 to 20 keV. Table 9 shows the ionization edge and characteristic peak energies of the elements.

Table 9: EDX energies (a) and EEL ionization edges (b) for the elements O, Na, Bi, Ti and Ba.

(a)		(b)	
Element	Energy [keV]	Element	Energy [eV]
O K	0.5	Ti L3	456
Na K	1.05	Ti L2	462
Bi M	2.5	O K	532
Ba L α	4.47	Ba M5	781
Ti K α	4.5	Ba M4	796
Bi L α	10.8	Na K	1072
Ba K α	32.2	Bi M5	2580
		Bi M4	2688

With EDXS, sodium, bismuth, titanium, oxygen and barium were identified. However, as already explained earlier in this chapter, the oxygen X-rays are partly absorbed by the sample which lowers the oxygen signal. Another problem occurs with titanium and barium, because there is an overlap of the Ba L and Ti K lines at 4.5 keV. If, however, Ba K, which lies at about 32 keV, is quantified and the ratio between Ba K and Ba L is known, Ba L can be calculated and subtracted from Ti K. In this spectrum image, however, the intensity of Ba K was so low that the signal was not distinguishable from noise. Hence, and due to the very high titanium intensity compared to the Ba intensity, the intensity of Ba L could be neglected in the quantification of Ti K. Barium as well as oxygen were therefore taken from the EEL spectra. The EEL barium signal was low compared to the oxygen and titanium signals. For titanium, the signals from both methods were quantified. Hence, titanium was used as reference for the other elements. To sum it up, sodium (Na K), bismuth (Bi M) and titanium (Ti K) were taken from the EDX spectra, while titanium (Ti L), oxygen (O K) and barium (Ba M) were taken from the EEL spectra.

Analysis of the spectra was done with the program *Digital Micrograph*. The background was corrected with an exponential model (*Power Law* model) in the case of EELS and with a linear model in the case of EDXS.

The measurement errors of the EDXS results were estimated from $2\sqrt{N}$ according to poisson statistics (N corresponds to the number of counts of each peak). The errors of the EELS results were calculated by the program and also lie in the range of $2\sqrt{N}$.

The results of the SI are depicted in Figure 26 as images of 18 x 6 pixels, each pixel corresponding to one measurement point in the spectrum image (compare Figure 25 (a)). The ratios of sodium, bismuth and oxygen with respect to titanium are shown. The values are depicted in a colour scale which ranges between 0.28 and 0.38 for Na:Ti, between 0.23 and 0.35 for Bi:Ti, between 3.02 and 3.35 for O:Ti and between 0.015 and 0.021 for Ba:Ti.

For Na:Ti, the error is approximately 9%, for Bi:Ti appr. 5%, for O:Ti appr. 10% and for Ba:Ti appr. 26%. The high error for Ba:Ti is based on the small barium signal. For Na:Ti and Bi:Ti, there is a gradient with higher values in the upper part of the investigated

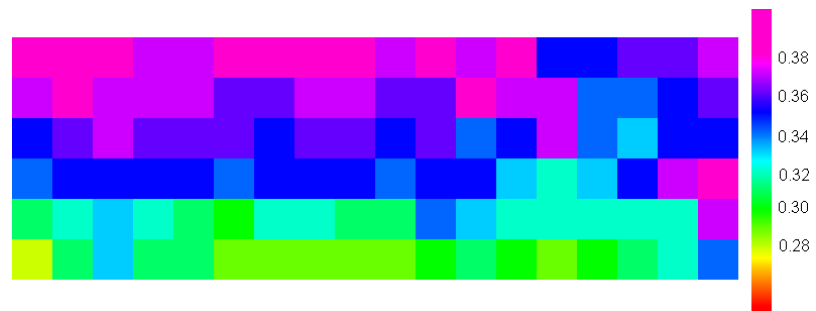
area and lower values in the lower part of the area. There are also measurement points with high values at the right boundary of the spectrum images of Na:Ti and Bi:Ti. Due to the depiction of the ratios, thickness effects of the sample are excluded. Although the investigated area looks inhomogeneous regarding the Ba:Ti ratio, no conclusion can be drawn concerning the homogeneity in this range due to the error of 26%. The same is true for O:Ti.

In Table 10, the nominal ratios calculated from the chemical formula for BNT-6BT are listed. Compared to the calculated ratios, the ratios of Na:Ti, Bi:Ti and Ba:Ti are lower than the expected values (see Table 10). This applies not only to the area investigated by means of spectrum image, but also to other examined areas on this sample (compare Figure 24). According to the calculations, there should be three times more oxygen than titanium in the sample, a value which is well represented by the measurements.

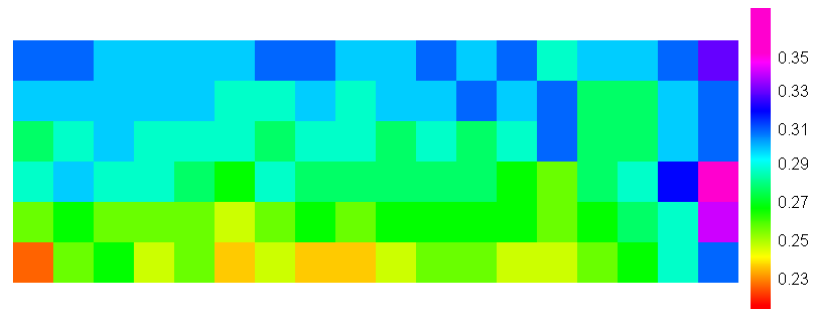
Table 10: Nominal values for Na, Bi, Ti, Ba and O according to the chemical formula for BNT-6BT in comparison to the experimental values.

Element	nominal [at%]	experimental [at%]
Bi	9,4	5,7
Na	9,4	6,8
Ti	20	20,8
O	60	66,4
Ba	1,2	0,4

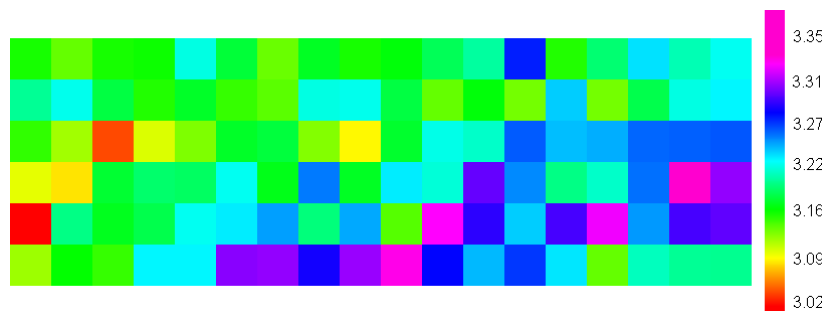
Ratios	nominal	experimental
Na-Ti	0,47	0,33
Bi-Ti	0,47	0,27
O-Ti	3,00	3,19
Ba-Ti	0,06	0,02



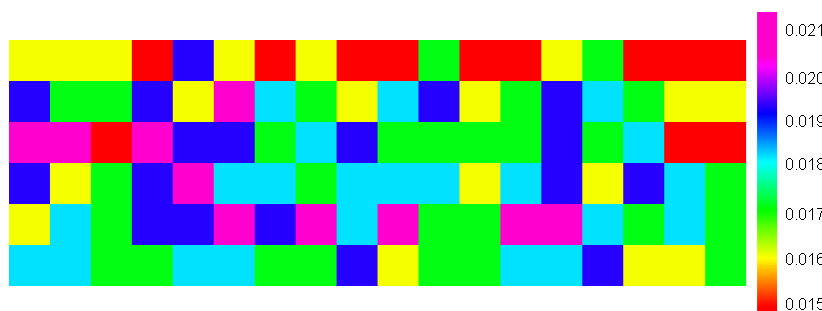
(a)



(b)



(c)



(d)

Figure 26: The images show the ratios of the concentrations in at% of (a) Na:Ti, (b) Bi:Ti, (c) O:Ti and (d) Ba:Ti of the spectrum image. The colour scale on the right of each image show the values which correspond to each colour.

5.3 Investigation of $(\text{Bi}_{0.5}\text{Na}_{0.35}\text{Li}_{0.15})\text{TiO}_3$

Like BNT-6BT, BNT-15BLT crystallizes in a perovskite structure (see Figure 4). BNT-15BLT was also examined by means of X-ray powder diffraction at the *Institute of Chemical Technology of Materials, TU Graz* and Rietveld refinement was done with the software *TOPAS*. The lattice parameters and atom coordinates of BNT-15BLT obtained from X-ray powder measurements are shown in Table 11. According to the X-ray data, the crystal system is rhombohedral with the space group R3c (161). For a phase diagram of BNT-15BLT see [26]. The specimen was investigated by means of powder electron diffraction as well as single crystal electron diffraction in order to examine the crystal structure and the homogeneity of the crystal structure. Additional information was obtained by bright field and dark field images. The chemical composition and homogeneity was investigated by EDXS and EELS measurements.

Table 11: Space group, lattice parameters and atom positions for the system BNT-15BLT obtained from X-ray analysis with a tetragonal structure model

Space group	R3c (161)				
Lattice parameters [Å]	a	5.4828			
	c	13.4907			
Atom positions		x	y	z	Occ
	Na	0.00000	0.00000	0.00000	0.35
	Bi	0.00000	0.00000	0.00000	0.50
	Li	0.00000	0.00000	0.00000	0.15
	Ti	0.00000	0.00000	0.23940	1
	O	0.35521	0.14940	0.14636	1

5.3.1 Powder electron diffraction

Like BNT-6BT, BNT-15BLT was investigated by means of powder electron diffraction. For information about the specimen preparation, see Chapter 4.2. The processing of the data was the same as for BNT-6BT (see Chapter 5.2). The results are depicted in Table 12, the powder pattern and its line profile are shown in Figure 27 (a) and

Table 12: Results of electron and X-ray powder diffraction for BNT-15BLT. The X-ray results are based on a rhombohedral structure model. (By courtesy of Denis Orosel, Institute of Chemical Technology of Materials, TU Graz)

electron diffraction		data from X-ray powder diffraction (rhombohedral)						
distance [1/nm]	d-spacing [Å]	d-spacing [Å]	Intensity	h	k	l	Mult.	2θ
3.62	2.76	27.496	5834956.63	-1	1	4	6	32.538
		27.414	5569526.01	-1	2	0	6	32.638
4.21	2.38	23.407	122402.08	-1	2	3	12	38.426
4.46	2.24	22.484	756799.29	0	0	-6	2	40.070
		22.395	2190924.43	-2	2	2	6	40.237
5.14	1.94	19.414	4313184.71	0	2	4	6	46.754
5.69	1.76	17.790	32754.32	-2	3	1	12	51.316
		17.385	557761.14	-1	2	6	12	52.602
		17.343	526336.86	-1	3	2	12	52.738
6.31	1.59	15.891	1211780.57	0	1	8	6	57.991
		15.843	2444757.20	-2	3	4	12	58.182
		15.827	1304695.36	0	3	0	6	58.246

(b), respectively. A comparison of X-ray data and the results from electron powder diffraction shows good agreement.

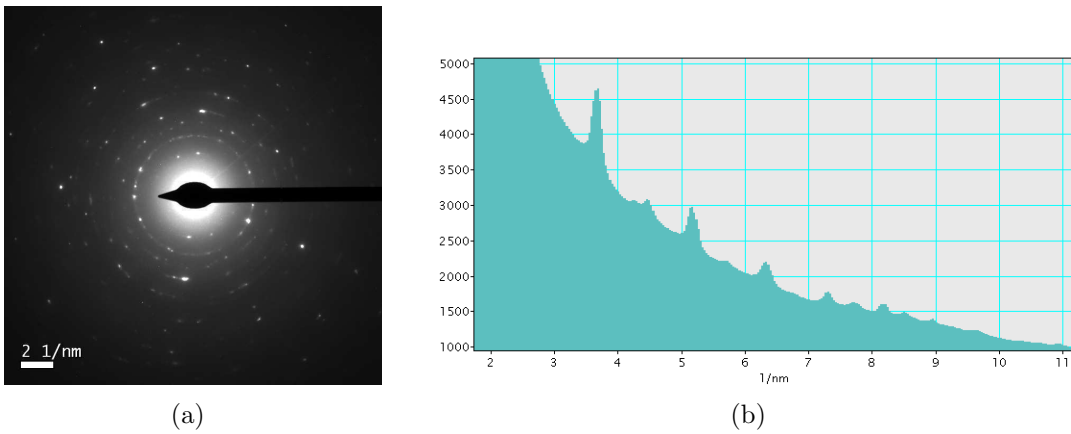


Figure 27: Powder pattern of BNT-15BLT (a) and line profile of the powder pattern (b)

5.3.2 Single crystal electron diffraction

Figure 28 (a) shows a rather large area of the sample in the orientation $[\bar{1}11]$. A set of contrast features is visible in this picture. On the one hand, there are typical bend contours which strongly change their appearance when the specimen is tilted. On the other hand, there are several clearly differentiated bands which are 150 to 550 nm wide (domains). In contrast to BNT-15BLT, domains were not found in BNT-6BT. In Figure 28 (b), the domains are depicted in a higher magnification.

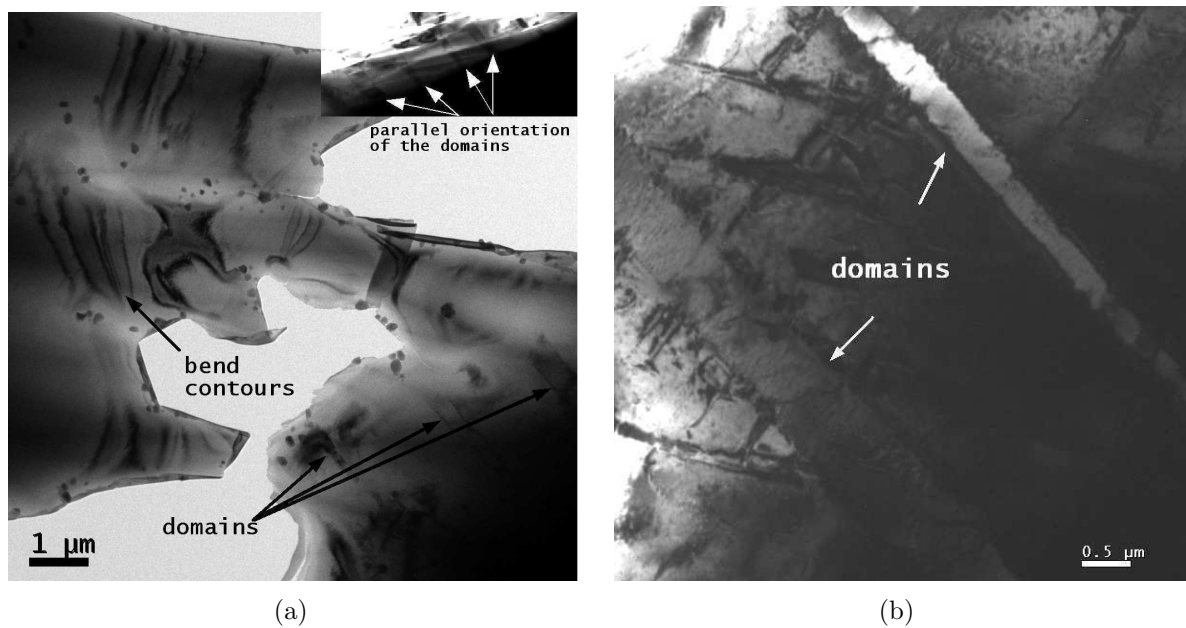


Figure 28: (a) Sample overview of BNT-15BLT. The contrast features are bend contours and domains. The parallel orientation of the domains is shown in the image in the upper right corner. (b) Domains depicted in a higher magnification. The images were acquired at the T 12.

In order to determine the crystal structure of the specimen a single crystal sample was investigated by means of electron diffraction. Figure 29 shows diffraction patterns in four different sample orientations. The diffraction pattern shown in Figure 29 (a) consists of reflections with higher and lower intensity. In this chapter, the reflections with higher intensity are referred to as type A reflections, those with lower intensity are referred to as type B reflections. Simulations with the software *JEMS* showed that the diffraction patterns in Figure 29 (b), (c) and (d) can either arise from a tetragonal

lattice or from a rhombohedral lattice. However, in contrast to a rhombohedral lattice, a tetragonal lattice won't show type B reflections in the diffraction pattern of Figure 29 (a). Hence, the diffraction pattern shown in Figure 29 (a) arises from a rhombohedral lattice (compare Chapter 5.2.2). According to the simulated pattern, the zone axis of this pattern is $[\bar{1}11]$. All diffraction patterns depicted in Figure 29 are obtained of the same sample area, just the tilt angle between the patterns differs. Hence, for the specimen BNT-15BLT only a rhombohedral phase was found.

The lattice parameters are depicted in Table 13. The values are compared to those obtained from XRD. The lattice constant a_r from TEM is $3.68 (\pm 0.05) \text{ \AA}$ and smaller than the one from XRD. As already mentioned for BNT-6BT, a much larger sample volume is examined by means of XRD. The angle α_r is also slightly smaller in TEM ($\alpha_r = 89.01 (\pm 0.05)^\circ$). Also shown in Table 13 are the lattice parameters of BNT-15BLT. Compared to BNT-6BT, a_r is smaller for BNT-15BLT, which was doped with the smaller ion lithium. BNT-6BT, in contrast, was doped with the larger ion barium. Comparison between the angles of BNT-6BT and BNT-15BLT obtained from XRD shows that the unit cell of the Li-doped sample is slightly distorted regarding a pseudo cubic unit cell in contrast to the Ba-doped sample. Due to the measurement error in TEM, no conclusion can be drawn from the TEM results.

Table 13: Lattice parameters for BNT-6BT and BNT-15BLT obtained from TEM diffraction patterns compared with XRD.

BNT-6BT	XRD	TEM
$a_r [\text{\AA}]$	3,90	3,88
$\alpha_r [^\circ]$	90,00	88,98
BNT-15BLT	XRD	TEM
$a_r [\text{\AA}]$	3,88	3,68
$\alpha_r [^\circ]$	89,83	89,01

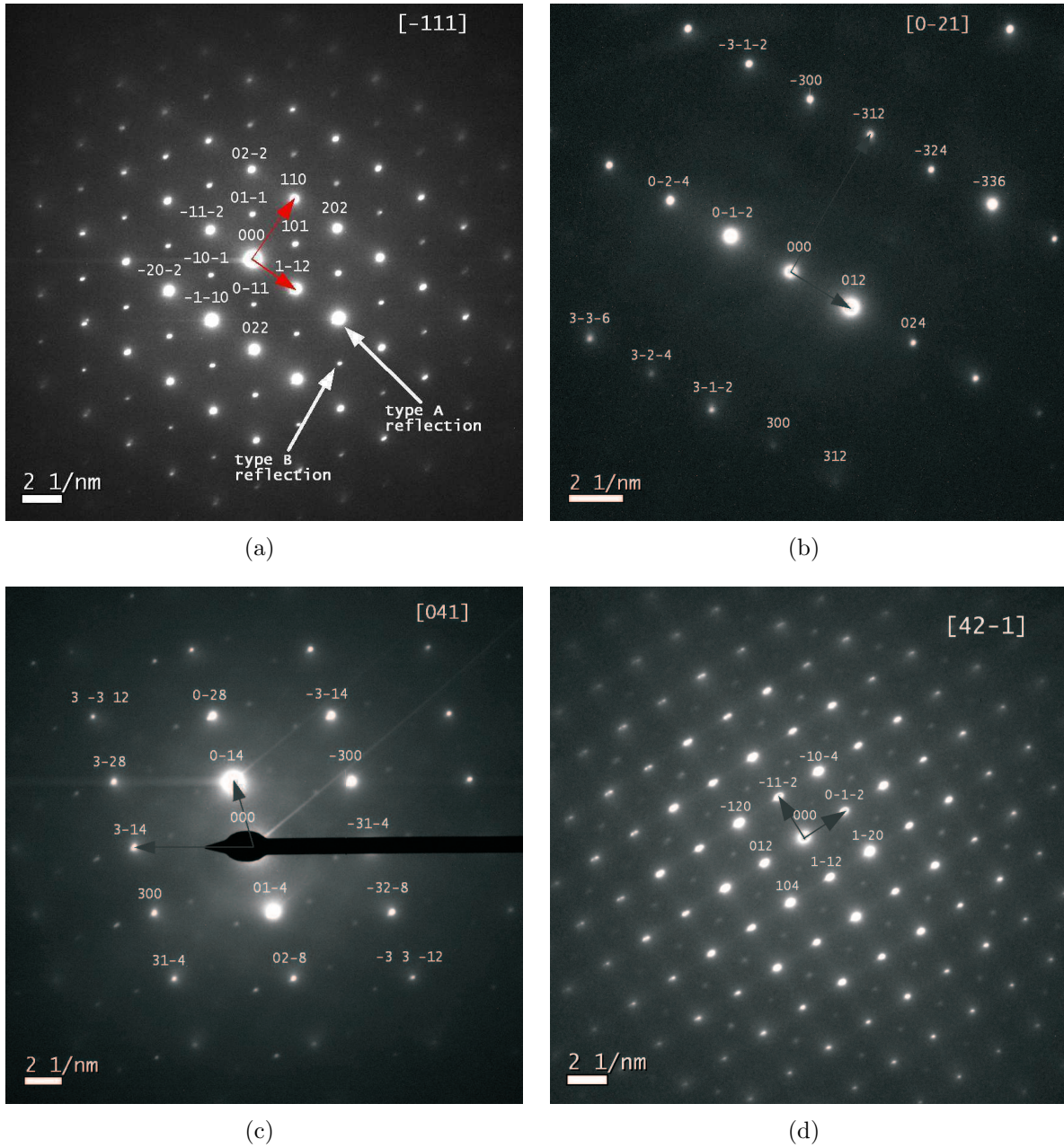


Figure 29: Single crystal diffraction patterns of BNT-15BLT in the orientations $[0\bar{2}1]$ (a), $[\bar{1}11]$ (b), $[041]$ (c) and $[42\bar{1}]$ (d) of a rhombohedral lattice. The diffraction patterns (a)-(c) were acquired at the T 12, (d) at the TF 20.

Investigation of domains. When a large SAED aperture was used, the diffraction patterns showed the same crystal structure all over the sample. However, the domains revealed in this sample were further investigated with small apertures (SAED) and small beam spot sizes (CBED) in order to reveal the source of contrast formation. The diffraction patterns acquired on the T 12, however, didn't show clear differences between the matrix and the domains. While the matrix showed a diffraction pattern as in Figure 29 (a), most of the type B reflections were absent in the diffraction pattern of the domains. As a second difference the domains showed satellite reflections and streaks, but the results were not reproducible. In order to obtain better results, the sample was investigated in the TF 20, which allows energy filtering.

First of all, dark field images were acquired to examine how the type A and type B reflections in Figure 29 (a) are related to the matrix and the domains. The dark field images as well as a bright field image are shown in Figure 30.

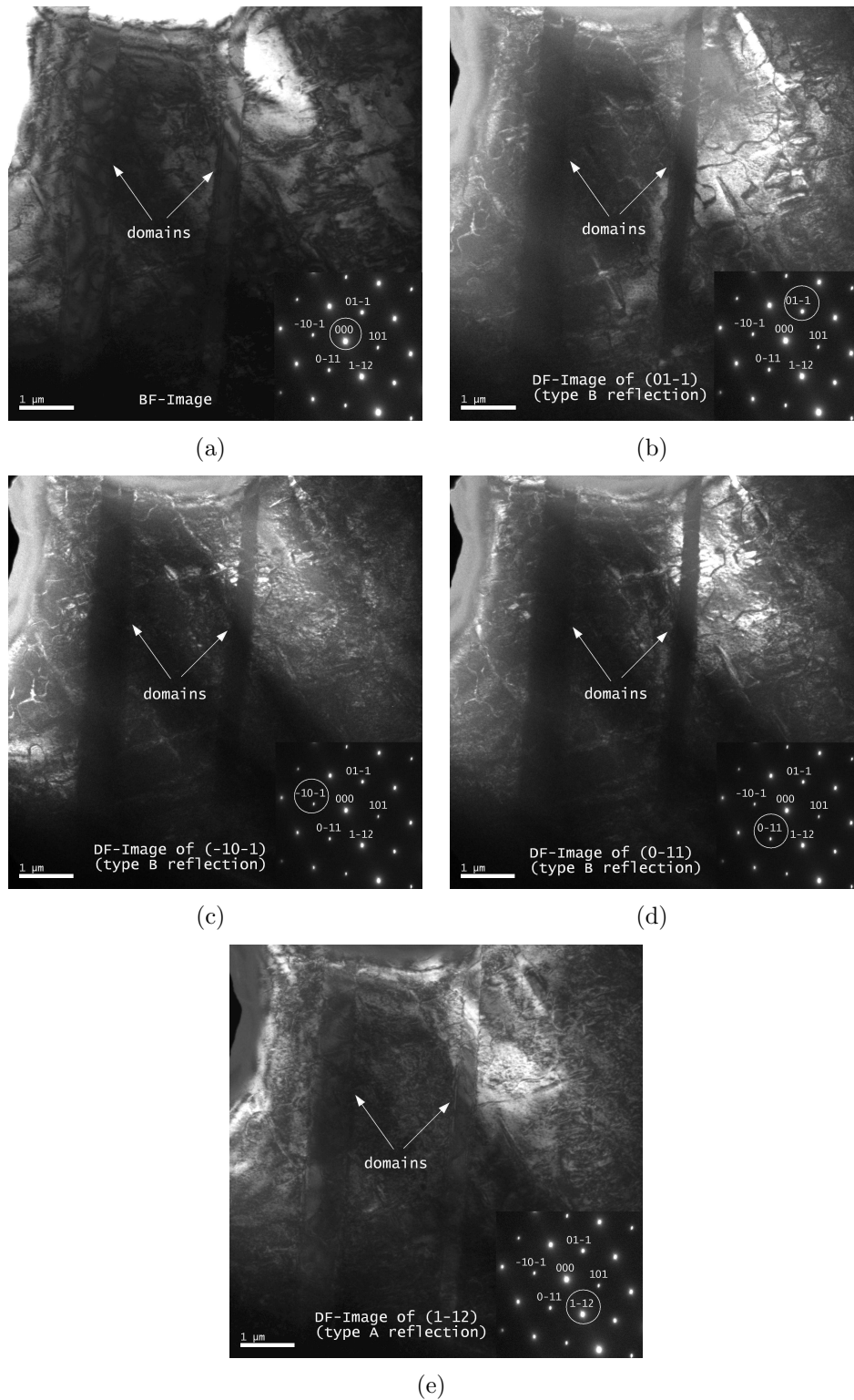


Figure 30: Dark and bright field images of a BNT-15BLT single crystal in the zone axis $[-111]$, acquired at the TF 20: DF images of type B reflections (a)-(c), DF image of a type A reflection (d), BF image (e). The diffraction pattern and the selected reflections are shown in the lower right corner of each image.

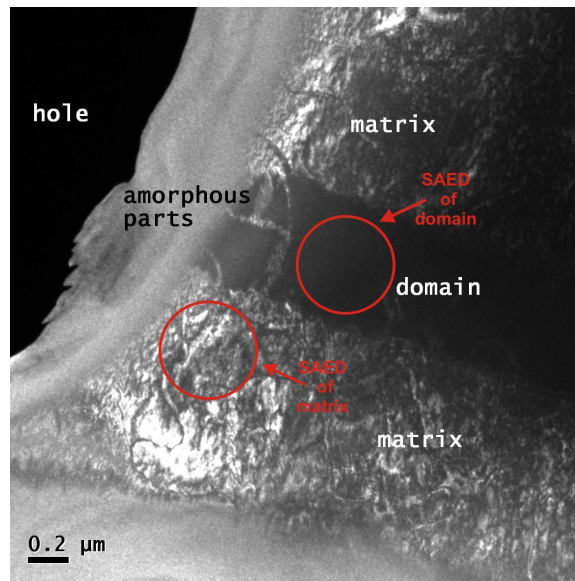


Figure 31: DF image showing the contrast between the matrix and the domain. The diffraction patterns shown in Figure 32 were acquired from the marked areas in the matrix and the domain region (TF 20).

The bright field image does not show big differences between the matrix and the domains. The dark field image of any of the type A reflections does not reveal big differences either. The dark field images of the type B reflections, however, show dark domains in a rather bright matrix. Nevertheless, the domains are not as dark as expected if no electrons were scattered from these regions. Figure 31 shows a dark field image at a higher magnification. The dark domain is clearly visible.

Diffraction patterns acquired from the smallest possible SAED aperture finally showed a clear difference between the matrix and the domain: while in the diffraction pattern of the matrix all reflections had roughly the same intensity (they showed an intensity ratio of 1:5 to 1:10), the diffraction pattern of the domain showed very sharp, but also very faint type B reflections coming along with the type A reflections. The intensities in this diffraction pattern showed an intensity ratio of 1:100. Now it becomes clear why the domains in the dark field images gained from the type B reflections appear darker, but not black: reflections of type b are found in the domains, but their intensity is very low. The two different diffraction patterns are shown in Figure 32.

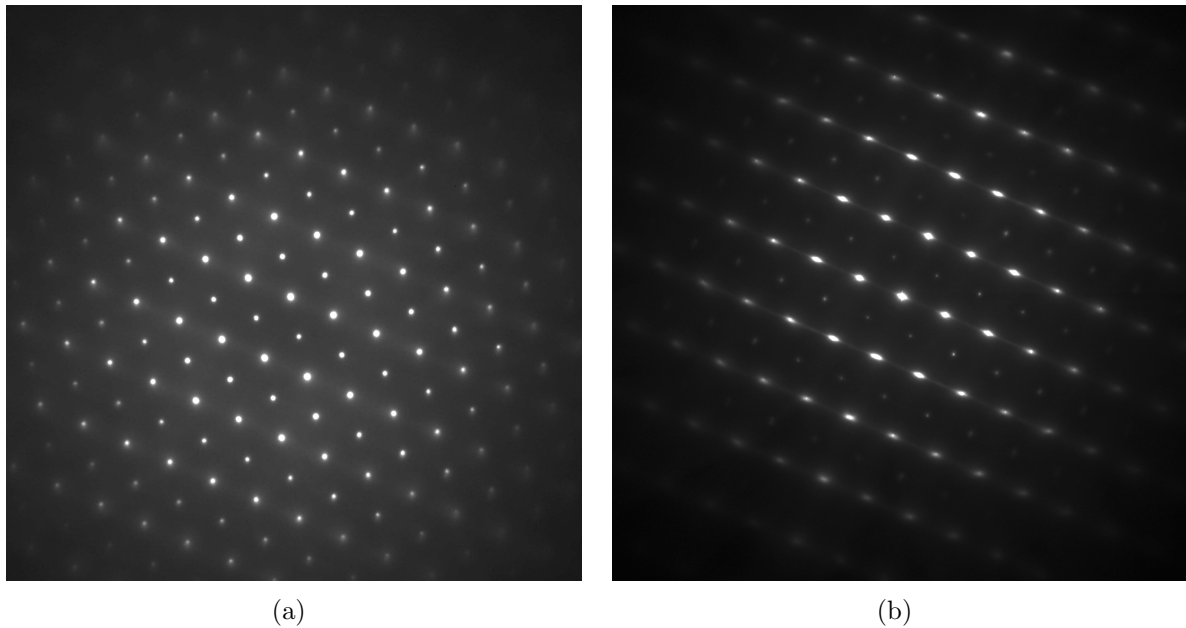


Figure 32: Difference between diffraction patterns of the matrix (a) and the domains (b): the type B reflections in the diffraction pattern of the domains are of very low intensity, the type A reflections are elongated to form streaks (TF 20).

There is, however, another difference between these two diffraction patterns: the domain is showing elongated type A reflections, so called streaks, while the matrix does not. In order to reveal the origin of the streaks, the area of the interface between the domain and the matrix was investigated by HRTEM (see Figure 33 (a)). The result is shown in Figure 33 (b): the domain on the lower right side of the picture seems to be built up of layers while the matrix does not. This layer composition gives rise to streaks in the diffraction pattern. The Fourier transformations (FT) of the domain and the matrix are also included and show the same features as explained before. The type B reflections are invisible in the FT due to their low intensity.

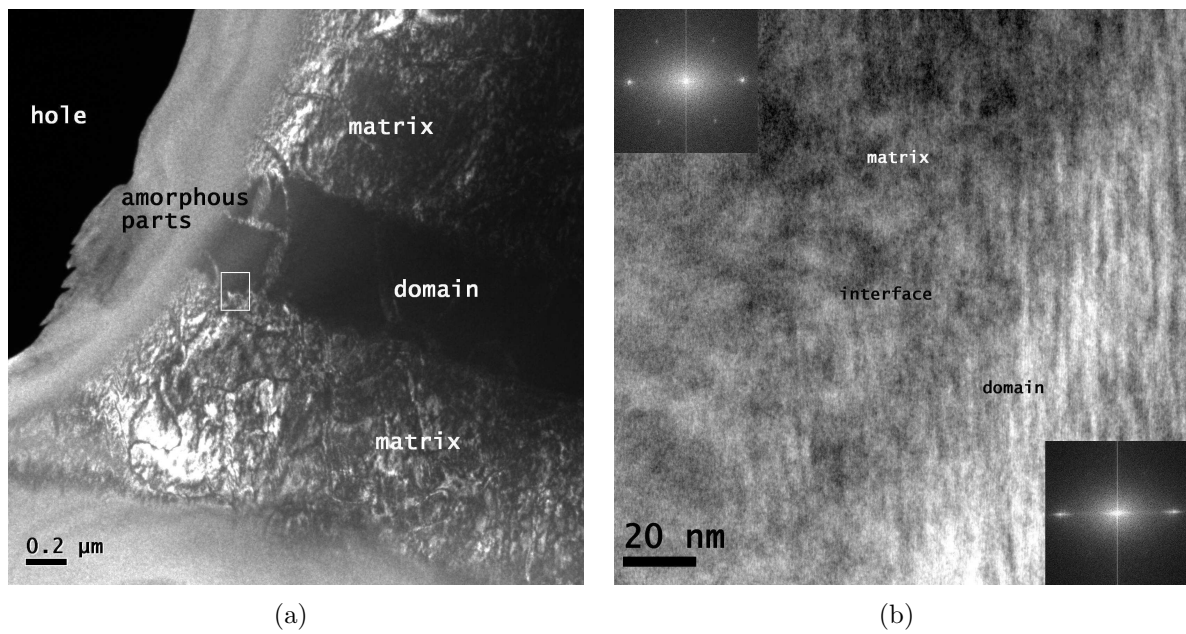


Figure 33: DF image showing the contrast between the matrix and the domain (a). The marked area corresponds to the high resolution image of the interface between matrix and domain shown in (b). The corresponding FTs are also depicted. The images were acquired at the TF 20.

5.3.3 Chemical analysis of BNT-15BLT

In order to investigate the distribution and homogeneity of the chemical elements within the sample, analytical measurements have been carried out.

All experiments concerning the chemical analysis of the sample were carried out on the CM 20. The samples were ion milled and investigated by means of EELS and EDXS measurements. Various regions of a sample of BNT-15BLT were investigated in STEM operation mode. The examined areas had a diameter of about 300 nm, as shown in Figure 34.

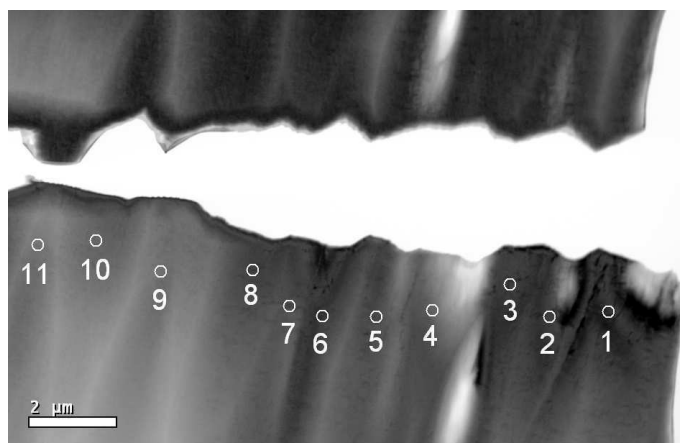


Figure 34: Investigated sample areas of BNT-15BLT

Although an oxygen peak occurs in the EDX spectrum, there is no reliable quantification of oxygen due to its low atomic number which leads to strong absorption of its X-ray photons in the sample. Oxygen, however, can be detected and reliably quantified by means of EELS. The same is true for lithium. For the detection and quantification of sodium and bismuth, EDX is the method of choice. Titanium is detected by both methods. For quantification, the Na K, Bi M and Ti K X-ray lines (EDXS) and the O K and Ti L ionization edges (EELS) were used. The EDX peak energies and EEL ionization edges are depicted in Table 14.

The EDX spectra were acquired in a 1-40 keV energy range using the software *NORAN System SIX (NSS)*. Quantification was also accomplished with NSS using experimental

Table 14: EDX energies (a) and EEL ionization edges (b) for the elements O, Na, Bi, Ti and Li.

(a)		(b)	
Element	Energy [keV]	Element	Energy [eV]
O K	0.5	Li K	60
Na K	1.05	Ti L3	456
Bi M	2.5	Ti L2	462
Ti K α	4.5	O K	532
Bi L α	10.8	Na K	1072
		Bi M5	2580
		Bi M4	2688

k-factors [21] (quantification fit method: Filter without standards, correction method: Cliff-Lorimer (MBTS) w/o absorbance). The EEL spectra were acquired and quantified using the software *Digital Micrograph*. The scattering cross-section model *hydrogenic (white line)* was applied for the quantification of titanium, the *Hartree-Slater model* for oxygen. The background was fitted according to a power law model. Before quantification, the EEL spectra were calibrated. Besides the core loss spectra, also the corresponding low loss spectra were acquired in order to determine the relative thickness of the investigated sample areas and to deconvolve the spectra when necessary. A deconvolution is required for sample areas thicker than 0.5 (relative thickness). The errors, which were calculated by the software, lie in the range of $2\sqrt{N}$, with N standing for the intensity or number of counts for each signal. All results are given in atomic percent.

Lithium could not be detected in TEM and STEM mode in the investigated samples. It is suggested that the sample preparation is the cause of this, because lithium is a very light element and hence is maybe ejected from the sample by the ion beam during ion milling. Figure 35 shows the ratios of bismuth, sodium and oxygen with respect to titanium. The ratios are used in order to be able to combine the results of both methods, EDXS and EELS. Titanium was chosen as a reference because it can be detected by both methods. The measurement points 1-11 correspond to the marked areas in Figure 34. The average value is indicated by a red line in each graph. The ratio of Bi:Ti looks quite stable within the investigated area, which is about $4 \times 16 \mu\text{m}^2$ in size. The same is true for the ratio of O:Ti. The ratio of Na:Ti, instead, is fluctuating in a bigger range around the average value.

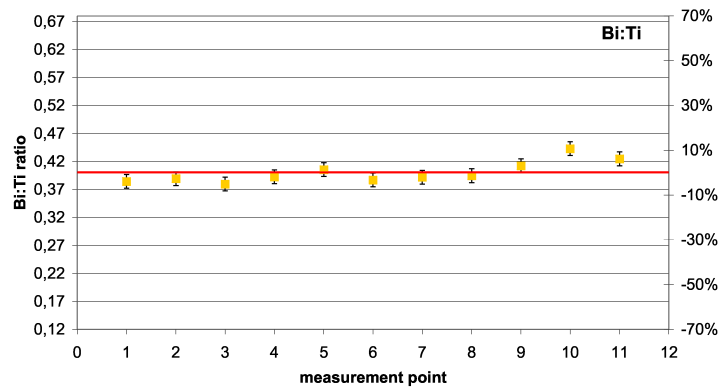
The results of both methods, EDXS and EELS, were then normalized to 100 per cent. Table 15 depicts the calculated values, according to the chemical formula, in atomic percent for each element as well as for the ratios. The experimental values are shown, too. The experimental average values are 63.7 (O), 8.4 (Bi), 7.0 (Na) and 21.0 (Ti). Compared to the calculated values, the amount of oxygen and titanium is slightly higher while the amount of bismuth is lower. The amount of sodium corresponds to the calculated value. Although the deviation would be small, it has to be considered that lithium was not taken into account when normalizing the other elements to 100 per cent.

Table 15: Nominal and experimental values for Na, Bi, Ti and O according to the chemical formula for BNT-15BLT.

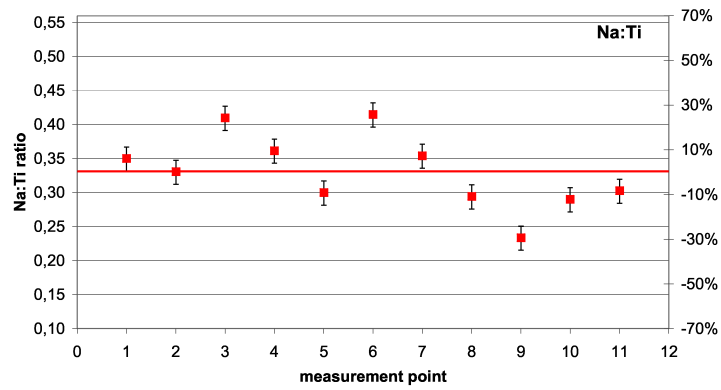
Element	nominal [at%]	experimental [at%]
Bi	10	8,4
Na	7	7
Li	3	-
Ti	20	21
O	60	63,7

Ratios	nominal	experimental
Na-Ti	0,35	0,33
Bi-Ti	0,50	0,40
O-Ti	3,00	3,03
Li-Ti	0,15	-

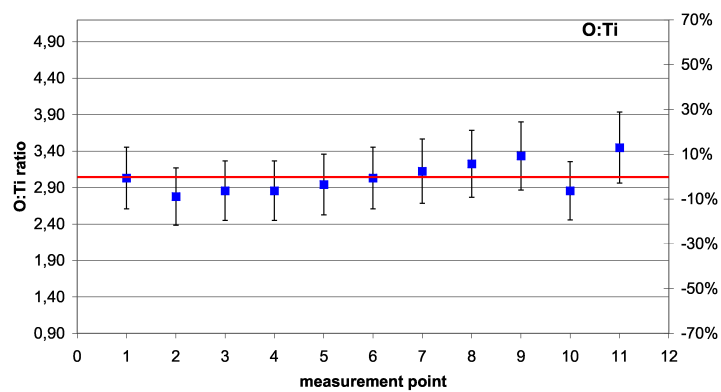
Additionally, each element is depicted in a separate graph in Figures 36 and 37. Concerning bismuth, titanium and oxygen, the sample is homogeneous in the investigated area. Sodium shows more fluctuations compared to the other elements.



(a)

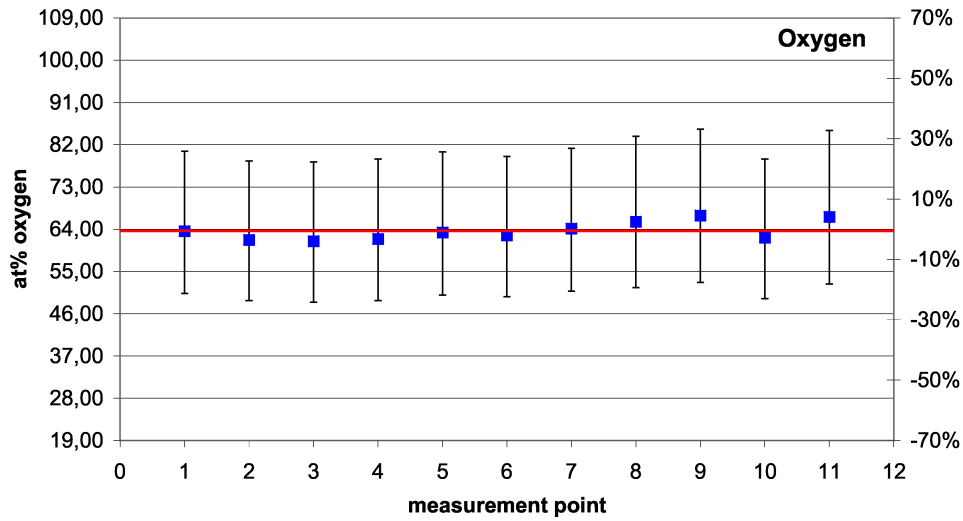


(b)

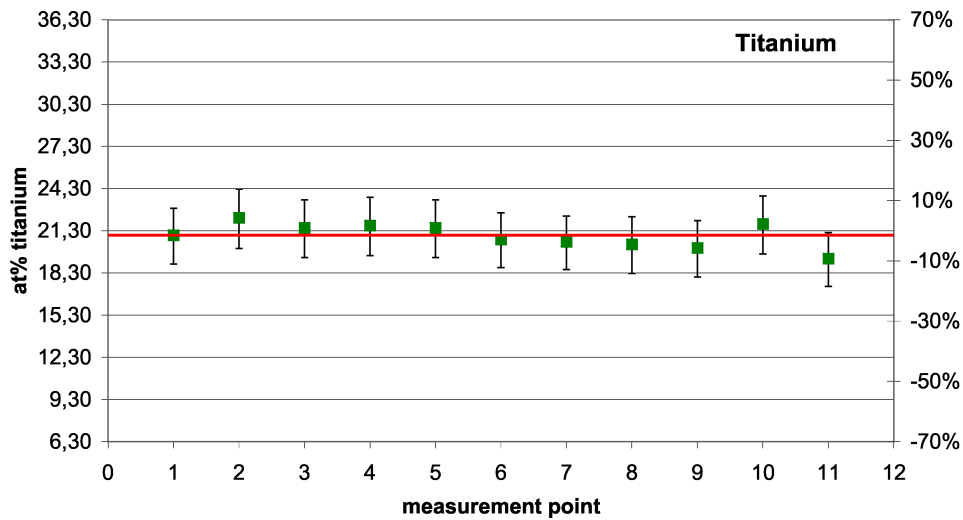


(c)

Figure 35: Ratio of (a) bismuth, (b) sodium and (c) oxygen with respect to titanium. The average value is indicated by a red line.

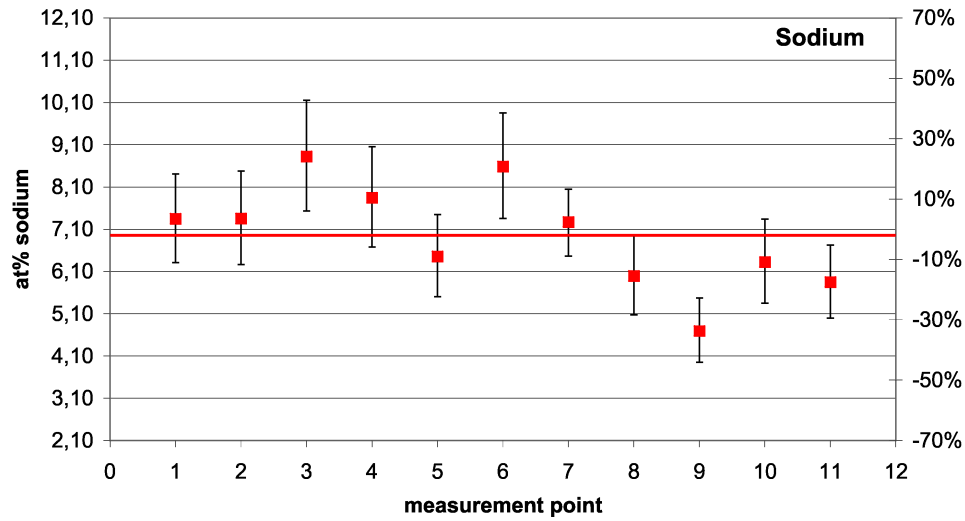


(a)

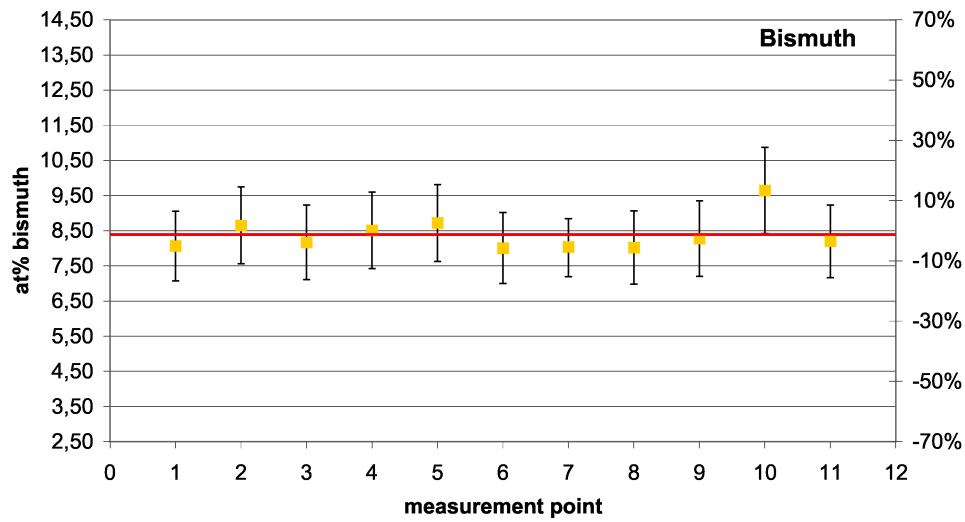


(b)

Figure 36: Amounts of oxygen and titanium in BNT-15BLT (red line: average value of all data points).



(a)



(b)

Figure 37: Amounts of sodium and bismuth in BNT-15BLT (red line: average value of all data points).

6 Summary

Two samples, BNT-6BT and BNT-15BLT, were investigated by means of powder electron diffraction as well as single crystal electron diffraction. Single crystal electron diffraction in combination with diffraction pattern simulations proved both samples to be rhombohedral. According to X-ray powder diffraction measurements, the crystallographic point group is $R3c$ in both samples. All examined sample areas were rhombohedral. The lattice parameters were determined with a_r being 3.88 Å for BNT-6BT and 3.68 Å for BNT-15BLT and α_r being 89° for both samples.

Bright field images approved the samples to be single crystals due to the absence of grain boundaries and showed BNT-6BT samples without any remarkable structures. BNT-15BLT, however, showed domains which were further investigated by means of dark field imaging and electron diffraction as well as HRTEM. The domains showed the same diffraction patterns as the matrix, differing only in the intensity of the reflections. Hence it was concluded that the domains feature the same crystal structure as the matrix. This was also illustrated by dark field images of the faint reflections. High resolution TEM revealed a layer structure of the domains in contrast to the matrix.

As far as the chemical composition is concerned, BNT-15BLT showed homogeneity of oxygen, titanium and bismuth in the investigated area, which was about $4 \times 16 \mu\text{m}^2$ in size. Sodium, instead, fluctuated slightly compared to the other elements. Lithium, however, could not be detected. Compared to the nominal values calculated on the basis of the chemical formula, the concentrations of sodium, titanium and oxygen correspond to the expected values. Only bismuth shows a concentration lower than the nominal one. For BNT-6BT, a EDX and EEL spectrum image was acquired. The results were depicted as ratios of Na, Bi, O and Ba with respect to titanium. It was shown that the values for O:Ti and Ba:Ti were ranging within the measurement errors and hence are homogeneous within these limits. For Na:Ti and Bi:Ti, the values showed a gradient over the investigated sample area. The ratios of Na:Ti, Bi:Ti and Ba:Ti are higher than the nominal ratios calculated on the basis of the chemical formula. Only the ratio of O:Ti corresponds to the nominal value.

List of Figures

1	Direct and inverse piezoelectric effect	8
2	Phase diagram of the system PZT	11
3	Phase diagram of the system BT	12
4	Unit cell of the perovskite structure	14
5	Bismuth-Layer-Structure	15
6	The structure of lithium niobate	16
7	Phase diagram of the binary system KNN	18
8	Phase diagram of the system BNT-BT	20
9	Definition of different planes in a lens system	21
10	Electron guns: thermionic gun and field emission gun	22
11	Restriction of the convergence angle of the beam by an aperture	23
12	The TEM illumination system	24
13	The TEM imaging system	25
14	Diffraction pattern	26
15	Electron diffraction modes	27
16	Dark field and bright field images	28
17	Sample preparation	34
18	Transmission electron microscopes	37
19	Particle of the investigated powder sample	40
20	Powder pattern of BNT-6BT	41
21	Bright field images of BNT-6BT showing a single crystalline specimen	43
22	Single crystal diffraction patterns of BNT-6BT	44
23	Comparison of simulated and acquired diffraction patterns	45
24	Investigation of the compositional stability of BNT-6BT	47
25	Spectrum Image of a sample of BNT-6BT	48
26	Na:Ti, Bi:Ti, O:Ti and Ba:Ti of the spectrum image	51
27	Powder pattern of BNT-15BLT	53
28	Sample overview of BNT-15BLT	54
29	Single crystal diffraction patterns of BNT-15BLT	56
30	Dark and bright field images of a BNT-15BLT single crystal	58
31	DF image showing the contrast between the matrix and the domain	59
32	Difference between diffraction patterns of the matrix and the domains	60

List of Figures

33	High resolution image of the interface between matrix and domains . . .	61
34	Investigated sample areas of BNT-15BLT	62
35	Ratio of bismuth, sodium and oxygen with respect to titanium.	65
36	Amounts of oxygen and titanium in BNT-15BLT	66
37	Amounts of sodium and bismuth in BNT-15BLT	67

List of Tables

1	Piezoelectric parameters of PZT	10
2	Starting materials for the preparation of BNT-6BT	32
3	Temperature program for the preparation of BNT-6BT crystals	33
4	Lattice parameters and atom positions for rhombohedral BNT-6BT	38
5	Lattice parameters and atom positions for tetragonal BNT-6BT	39
6	Electron and X-ray powder diffraction for rhombohedral BNT-6BT	41
7	Electron and X-ray powder diffraction for tetragonal BNT-6BT	42
8	Lattice parameters for BNT-6BT	45
9	EDX energies and EEL ionization edges for BNT-6BT	48
10	Nominal and experimental values for BNT-6BT	50
11	Lattice parameters and atom positions for the system BNT-15BLT	52
12	Electron and X-ray powder diffraction for BNT-15BLT	53
13	Lattice parameters for BNT-6BT and BNT-15BLT	55
14	EDX energies and EEL ionization edges for BNT-15BLT	63
15	Nominal and experimental values for BNT-15BLT	64

References

- [1] <http://www.rohs.eu> (as at October 2010)
- [2] A.J. Moulson, J.M. Herbert: *Electroceramics*, 2nd edition, Wiley (2003)
- [3] H. Schaumburg (Hrsg.): *Keramik - Werkstoffe und Bauelemente der Elektrotechnik*, Band 5, B.G. Teubner Stuttgart (1994)
- [4] <http://www.pic ceramic.com> (as at October 2010)
- [5] J. Ricote, R.W. Whatmore, D.J. Barber: Studies of the ferroelectric domain configuration and polarization of rhombohedral PZT ceramics, *J Phys.: Condens. Matter* **12** (2000), 323-337
- [6] Z.H. Zhang, X.Y. Qi and X.F. Duan: Two-step evolution mechanism of multi-domains in BaTiO₃ single crystal investigated by in situ transmission electron microscopy, *Scripta Materialia* **58** (2008), 441-444
- [7] J. Rödel, W. Jo, K. Seifert, E. Anton, T. Granzow, D. Damjanovic: Perspective on the Development of Lead-free Piezoceramics, *Journal of the American Ceramic Society*, **92** [6] (2009), 1153-1177
- [8] T. Takenaka, H. Nagata: Current status and prospects of lead-free piezoelectric ceramics, *Journal of the European Ceramic Society* **25** (2005) 2693-2700
- [9] P.K. Panda: Review: environmental friendly lead-free piezoelectric materials, *Journal of the Materials Science*, **44** (2009), 5049-5062
- [10] R. Ranjan, A. Dviwedi: Structure and dielectric properties of (Na_{0.50}Bi_{0.50})_{1-x}Ba_xTiO₃, *Solid State Communications* **135** (2005), 394-399
- [11] V.M. Goldschmidt, *Geochemische Verteilungsgesetze der Elemente. VII: Die Gesetze der Kristallochemie*, *Skifter utgitt av det Norske Videnskaps-Akademi i Oslo*, **2** (1926), 5-116
- [12] K. Hansen, K. Astafiev, T. Zawada: Lead-free piezoelectric thick films based on potassium sodium niobate solutions, in *Proceedings of the 2009 IEEE International Ultrasonics Symposium*, 1738-1741
- [13] ACerS-NIST Phase Equilibria Diagram Database (as at October 2010)

-
- [14] V. Dorcet, G. Trolliard, P. Boullay: The structural origin of the antiferroelectric properties and relaxor behavior of $\text{Na}_{0.50}\text{Bi}_{0.50}\text{TiO}_3$, *Journal of Magnetism and Magnetic Materials* **321** (2009), 1757-1761
- [15] V. Dircet, G. Trolliard, P. Boullay: Reinvestigation of Phase Transitions in $\text{Na}_{0.50}\text{Bi}_{0.50}\text{TiO}_3$ by TEM: Part I: First Order Rhombohedral to Orthorhombic Phase Transition, *Chem. Mater.*, **20** (2008), 5061-5073
- [16] M. Otonicar, S.D. Skapin, M. Spreitzer, D. Suvorov: Compositional range and electrical properties of the morphotropic phase boundary in the $\text{Na}_{0.50}\text{Bi}_{0.50}\text{TiO}_3$ - $\text{K}_{0.50}\text{Bi}_{0.50}\text{TiO}_3$ system, *Journal of the European Ceramic Society* **30** (2010), 971-979
- [17] V.A. Shuvaeva, D. Zekria, A.M. Glazer, Q. Jiang, S.M. Weber, P. Bhattacharya, P.A. Thomas: Local structure of the lead-free relaxor ferroelectric $(\text{K}_x\text{Na}_{1-x})_{0.5}\text{Bi}_{0.5}\text{TiO}_3$, *Physical review B* **71** (2005), 174114
- [18] Q. Xu, X. Chen, W. Chen, B. Kim, S. Xu, M. Chen: Structure and electrical properties of $(\text{Na}_{0.50}\text{Bi}_{0.50})_{1-x}\text{Ba}_x\text{TiO}_3$ ceramics made by a citrate method, *J Electroceram*, **21** (2008), 617-620
- [19] T. Takenaka, K. Maruyama, K. Sakata: $\text{Na}_{0.50}\text{Bi}_{0.50}\text{TiO}_3$ - Ba_xTiO_3 System for Lead-Free Piezoelectric Ceramics, *Jpn. J. Appl. Phys., Part 1*, **30** [9B] (1991), 2236-9
- [20] D.B. Williams, C.B. Carter: *Transmission Electron Microscopy, Part 1-4*, 2nd edition, Springer (2009)
- [21] W. Grogger: *Quantitative Mikrobereichsanalyse im Analytischen Elektronenmikroskop unter Verwendung eines HPGe-Röntgendetektors*, Dissertation (1994)
- [22] M. De Graef: *Introduction to Conventional Transmission Electron Microscopy*, Cambridge (2003)
- [23] B. Fulz, J.M. Howe: *Transmission Electron Microscopy and Diffractometry of Materials*, Springer (2001)
- [24] M. Heimendahl: *Electron Microscopy of Materials*, Academic Press (1980)
- [25] ICSD Database (as at October 2010)
- [26] Y. Hiruma, K. Yoshii, H. Nagata, T. Takenaka: Phase transition temperature and electrical properties of $(\text{Bi}_{0.50}\text{Na}_{0.50})\text{TiO}$ - $(\text{Bi}_{0.50}\text{A}_{0.50})\text{TiO}$ (A=Li and K) lead-free ferroelectric ceramics, *Journal of Applied Physics* **103**, 084121 (2008)